Structural Insights into the Electrostatic interactions in Human Serum Albumin dimerization patterns and dipyridamole interaction.

by

Haluk Çetinok

A Dissertation Submitted to the
Graduate School of Sciences and Engineering
in Partial Fulfillment of the Requirements for
the Degree of
Master of Science
in
Molecular Biology and Genetics

KOÇ ÜNİVERSİTESİ

22 May, 2025

Structural Insights into the electrostatic interactions in Human Serum Albumin dimerization patterns and dipyridamole interaction

Koç University

Graduate School of Sciences and Engineering

This is to certify that I have examined this copy of a master's thesis by

Haluk Çetinok

and have found that it is complete and satisfactory in all respects,
and that any and all revisions required by the final
examining committee has been made.

Committee Members:

_____
Asst. Prof. Hasan Demirci

_____
Prof. Dr. Erol Erçağ

_____
Asst. Prof. Eda Yıldırım

Date: _____

To all that consider me family…

ABSTRACT

Structural Insights into the electrostatic interactions in Human Serum Albumin dimerization patterns and dipyridamole interaction

Haluk Çetinok

Master of Science in Molecular Biology and Genetics

May 22, 2025

Human serum albumin (HSA) is a ubiquitous, multifunctional protein responsible for the body-wide distribution of both endogenous metabolites' nutrients and exogenous pharmaceuticals. Its inherent properties, mainly its ability to transcytosis and leak into the tissue lumens and having multiple ligand-binding sites, have rendered HSA an exploitable building block in nanoparticle-based drug delivery systems, particularly in cancer targeting. In this study, we present high-resolution crystallographic data (PDB ID: 9V61) supported structure revealing two distinct dimerization patterns of HSA, obtained under high-concentration crystallization conditions, in addition to results from dipyridamole dockings. Both dimer types demonstrate extensive interface areas and a significant number of electrostatic interactions. Comparative analysis with previously reported dimer structure (3JQZ) and other high-interface-area structures, (5Z0B, 8CKS) indicate similarities in contact regions, but unique residue-level differences in biophysical electrostatic bonding interactions. Interface surface area distribution and space group histograms further support the rarity and potential therapeutic relevance of the identified dimer forms. Importantly, these dimer configurations do not disrupt Sudlow's drug-binding sites, which is important as the dipyridamole docking analysis presents a strong affinity to Sudlow site I, not affecting their utility in engineered drug delivery. Our findings open new avenues for structure-based mutagenesis and nanoparticle design strategies centered on HSA dimerization dynamics.

ÖZETÇE

İnsan Serum Albümininin Dimerleşme ve Dipiradamol Bağlanmasının Yapısal İncelemesi

Haluk Çetinok

Moleküler Biyoloji ve Genetik Yüksek Lisans

22 Mayıs 2025

İnsan serum albümini (HSA), hem endojenik metabolitlerin ve besinlerin, hem de eksojenik ilaç gibi maddelerin vücut genelinde dağılımı sağlayan, kan serumunda ve doku boşluklarında diğer proteinlere göre yüksek miktarda bulunan ve birden çok işlevi olan bir proteindir. Transsitoz yapabilme ve doku lümenlerine sızabilme özelliklerinin yanı sıra çok miktarda farklı ligand bağlanma bölgelerine sahip olması, HSA'yı özellikle kanser hedeflemede nanoparçacık temelli ilaç taşıma sistemlerinde kullanılabilir bir yapı taşı haline getirmiştir. Bu çalışmada, yüksek konsantrasyonlu kristalleşme koşullarında elde edilen (PDB ID: 9V61), HSA'nın iki farklı dimerleşme modelini ortaya koyan yüksek çözünürlüklü kristalografik verilerine dayalı bir yapı sunulmasına ek olarak; dipiridamol bağlanma simülasyon analizlerinin sonuçlarını da verilmektedir. Her iki dimer tipi de geniş ara yüzey alanları ve çok sayıda elektrostatik etkileşim göstermektedir. Önceden bildirilmiş dimer yapısı (3JQZ) ve benzer yükseklikteki ara yüzey alanına sahip diğer yapılarla (5Z0B, 8CKS) yapılan karşılaştırmalı analizler, temas bölgelerinde benzerlikler olduğunu, ancak elektrostatik bağlanma etkileşimlerinde farklılıklar bulunduğunu göstermektedir. Ara yüzey alanı dağılımı ve uzay grubu histogramları, belirlenen dimer formlarının nadirliğini ve potansiyel terapötik önemini daha da desteklemektedir. Önemli olarak, bu dimer konfigürasyonları Sudlow'un ilaç bağlanma bölgelerinin yapısını ve şeklini etkilememektedir; bu da, dipiridamol bağlanma analizinin Sudlow bölgesi I'e güçlü bir bağlanma eğilimi gösterdiği dikkate alındığında, bu dimerleşme yapıları temel alan mühendislik ürünü ilaç taşıma sistemlerinin ilaç bağlanma kuvveti ve miktarının düşmeyeceğini göstermektedir. Bulgularımız, yapıya dayalı mutajene ve HSA dimerleşme dinamiklerine odaklı nanoparçacık tasarım stratejileri için yeni yollar açmaktadır.

ACKNOWLEDGMENTS

I am very grateful to Asst. Prof. Hasan Demirci whose support and guidance have been instrumental in my academic progress.. I would also like to thank the members of my thesis committee, Asst. Prof. Eda Yıldırım and Prof. Dr. Erol Erçağ. Additionally, I would like to thank Assoc. Prof Veyis Karakoç for his support of the research that became this thesis. I also carry deep gratitude toward the members of the Kuybiig-M family and my dearest colleagues who deserve to be named: Alaleh Shafiei, Ayça İrgit, Betül Ertem, Bilge Tosun, Cahine Kulakman, Cengiz Kaan Ferah, Ebru Destan, Ece Akyüz, Eda Topalan, İlkin Yapıcı, Jerome Austin Johnson, Necati Atalay, Ömür Güven, Seyide Seda Paydos and Zeliş Nergis. No words would be enough to convey my gratitude toward my parents who made this dream possible, Gamze and Serdar Çetinok.

TABLE OF CONTENTS

LIST OF TABLES

LIST OF FIGURES

ABBREVIATIONS

Arg	Arginine
Asn	Asparagine
Asp	Aspartic acid
BME	2-Mercaptoethanol
cAMP	cyclic adenosine monophosphate
cGMP	cyclic guanosine monophosphate
cryo-EM	Cryogenic electron microscopy
DNA	Deoxyribonucleic acid
DTT	dithiothreitol
ENT1	Equilibrative nucleoside transporter 1
FPLC	Fast protein liquid chromatography
Gln	Glutamine
Glu	Glutamic acid
gp60	Glycoprotein 60KDa
His	Histidine
HSA	Human Serum Albumin
Leu	Leucine
Lys	Lysine
NMR	Nuclear magnetic resonance
PAGE	Polyacrylamide gel electrophoresis
PDB	Protein Databank
PEG	Polyethylene glycol
RMSD	Root mean square deviation
SDS	Sodium dodecyl sulfate
SEC	Size exclusion chromatography
Ser	Serine
SPARC	secreted protein acidic and rich in cysteine
Thr	Tryptophane
Tyr	Tyrosine
Val	Valine

XRD	X-ray diffractometer

Chapter 1

INTRODUCTION

1.1 Human Serum Albumin

Human serum albumin (HSA) is an abundantly found globular serum protein produced in the liver which plays a crucial role in transporting metabolites and drug active ingredients throughout the human body (Afrin et al., 2022). Even though the name may suggest it predominantly localizes intravascularly, HSA is most abundant in extravascular space distributed in tissues and secretions (Merlot et al., 2014). HSA with a half-life of 19 days approximately completes 28 cycles of dislocating into the tissues and returning to the vascular system via lymphatic vessels (Afrin et al., 2022), (Merlot et al., 2014)). In addition to the nutrients, HSA also carries a significant number of exogenous components including the majority of prescribed drugs (Zhivkova, 2015).

Structurally HSA exists as a collection of α-helices (67% α-helices, 10% turns, 23% random coils) exclusively having two main drug binding sites, seven fatty acid binding sites, and two nucleic acid binding sites. ((Mishra & Heath, 2021), (Alinovskaya et al., 2018)]. Figure 1 shows the scheme summarizing the versatility of HSA highlighting some of its many ligands. HSA binding is a dynamic process consisting of the equilibrium between the association and dissociation of ligands thus is dictated by the ligand concentration and free HSA amounts in the specific tissue, for example as HSA carries the toxic bilirubin to the liver, only 20% of the bilirubin bound to HSA is loaded off in the hepatic capillaries per cycle demonstrating how albumin transportation occurs (Kalakonda et al., 2022).

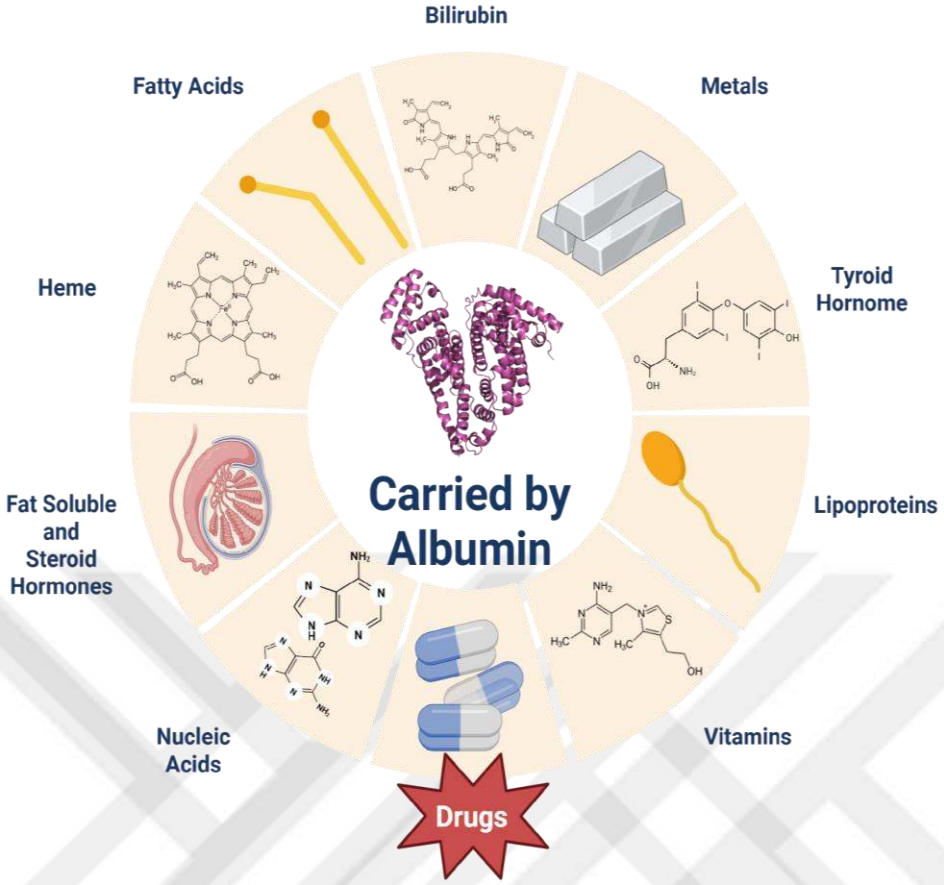

Figure 1.1: Scheme of some of the metabolites carried by or interacting with HSA. Starting at the top clockwise; Bilirubin, metals, thyroid hormone, lipoproteins, vitamins, drugs, nucleic acids, fat-soluble and steroid hormones, heme, and fatty acids.

The tissue presence is mainly attributed to the caveolin-dependent Albondin and glycoprotein 60KDa (gp60) mediated transcytosis actively translocating albumin in the capillary lumen to the tissue lumen in order to also transport the nutrients albumin carries into those tissues (Chinnaswamy Tiruppathi et al., 1997). As HSA is an important and ample nutrient carrier, multiple types of cancer overexpress the gp60 receptors to better syphon those nutrients rendering HSA an inherently cancer-targeting molecule (Ji et al., 2024), (Patel et al., 2021). This disproportionate targeting has given rise to an altogether different area, HSA nanoparticles (Qu et al., 2024). HSA nanoparticles (either completely made of HSA or covered with HSA) have at least a 2-fold accumulation in tumor tissues

as opposed to similar-sized HAS-less nanoparticles (Wei et al., 2023). Those nanoparticles can be done via either crosslinking or partially denaturing and renaturing HSA in high concentrations hence HSA self-interactions and multimerization can play an important role in the properties of those nanoparticles (Wei et al., 2023). HSA consists of three homologous domains each consisting of a double repeating segment kept together via 17 disulfide bridges as presented in Figure 2. The helices are named depending on their locations regarding those domain repeats.

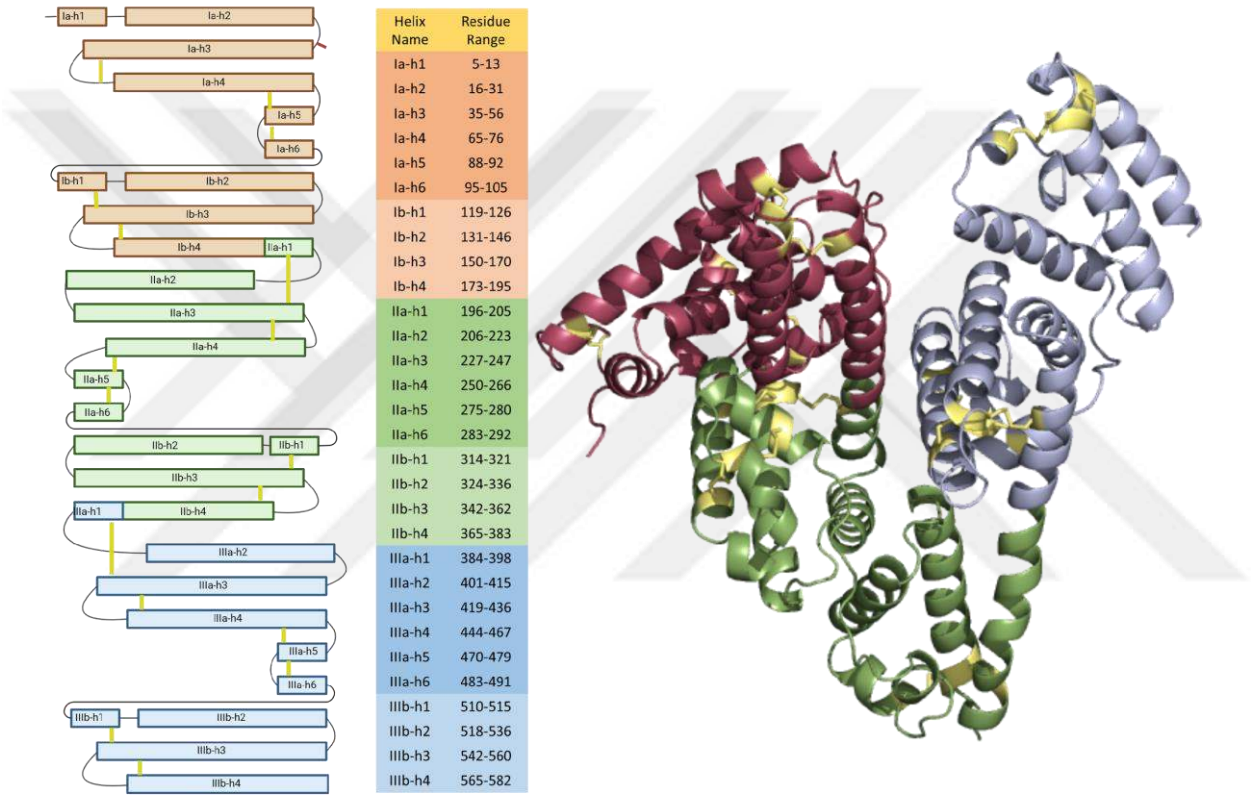

Helix Name	Residue Range
Ia-h1	5-13
Ia-h2	16-31
Ia-h3	35-56
Ia-h4	65-76
Ia-h5	88-92
Ia-h6	95-105
Ib-h1	119-126
Ib-h2	131-146
Ib-h3	150-170
Ib-h4	173-195
IIa-h1	196-205
IIa-h2	206-223
IIa-h3	227-247
IIa-h4	250-266
IIa-h5	275-280
IIa-h6	283-292
IIb-h1	314-321
IIb-h2	324-336
IIb-h3	342-362
IIb-h4	365-383
IIIa-h1	384-398
IIIa-h2	401-415
IIIa-h3	419-436
IIIa-h4	444-467
IIIa-h5	470-479
IIIa-h6	483-491
IIIb-h1	510-515
IIIb-h2	518-536
IIIb-h3	542-560
IIIb-h4	565-582

Figure 1.2: Map of HSA The domains and the helices of human serum albumin with indicated cysteine disulfide bridges are presented. The protein structure presented is the solved structure's chain A. The subdomains are differentiated via color and the cysteine bridges are placed in their approximate locations.

Both within those repeats and between them there are multiple binding sites for metabolites and drugs (Merlot et al., 2014). The metabolites and drugs with deposited crystal structures in the Protein Data Bank (PDB) have been aligned to our solved structures Chain A to emphasize the wide distribution of those binding sites on the protein

in Figure 3. Fatty acids, drugs, metabolites (like heme and bilirubin), and metals can bind to multiple sites on the protein making every part of its surface relevant for drug transporting and nanoparticle-forming procedures.

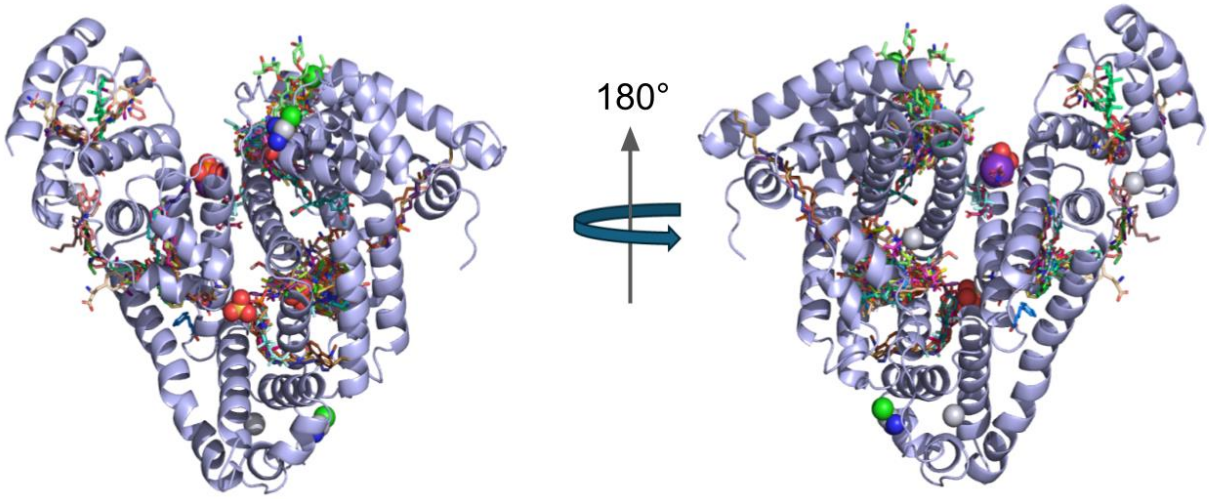

Figure 1.3: HSA with structurally determined load. Most known ligands of human serum albumin demonstrated in PDB deposited structures (over 100) aligned to our structure's chain A emphasizing the versatility and the spread of binding sites on the protein.

HSA can also interact with other proteins as well (Gurung et al., 2021), and in blood, 5% of the total HSA is found in a covalent dimeric form with a disulfide bridge between two HSA monomers at their own Cyc34 residues (Harris et al., 2024), (Chubarov et al., 2020). Even though there is little evidence of HSA forming reversible dimers in physiological conditions (Harris et al., 2024), (Chubarov et al., 2020), recombinantly dimerized HSA and HSA multimerized in nanoparticles has higher drug targeting efficiency (Taguchi et al., 2012) hence artificial and/or in vivo dimerization patterns may be utilized for improving nanoparticle efficiency and play a role in mutagenesis targeting. In crystallization, the dimers occurring can either have biological significance or be a crystallization artifact, usually, the area of the interface between the monomers of the

dimer and the interaction strength differentiates between them (Yueh et al., 2017). Non-biological dimer interfaces tend to be smaller (<1000 Å) with little electrostatic interactions. The only other established HSA reversible dimer (PDB accession code: 3JQZ) has a similar surface area to our interfaces (1718.9Å to 1695.1Å) and comparable electrostatic interactions (28 to 24) (Kim Langmach Hein et al., 2010). While usually the driving force between protein dimers is hydrophobic interactions, the interaction being forced by electrostatic interaction, especially on higher concentrations, is not unheard of (Bjørk et al., 2003). As HSA dimerization and self-interactions can influence both nanoparticle dynamics and targeting properties, discovering possible dimerization patterns could introduce new parameters to both fields as mutagenesis targets and may offer insights into new conditions in which the HSA nanoparticles could be generated.

Human serum albumin (HSA) contains several binding regions, as shown in Figure 1, with different properties that make this protein a significant factor for drug distribution in the bloodstream, as several pharmaceutical drugs tend to bind to specific regions of the protein. For instance, drugs such as warfarin or phenylbutazone have a higher affinity towards Sudlow Site I. On the other hand, diazepam, ibuprofen, or naproxen demonstrate a higher affinity towards Sudlow site II (Ghuman et al., 2005) (Sudlow et al., 1975). In the present study, molecular docking simulations of dipyridamole have been performed at the Sudlow Site I of the IIA subdomain of HSA.

1.2 Dipyridamole

The drug active ingredient dipyridamole is mainly prescribed as an antiplatelet agent as one of its functions is inhibiting phosphodiesterase leading to the accumulation of signaling molecules cAMPs (cyclic adenosine monophosphate) and cGMP's (cyclic

guanosine monophosphate) hence inhibiting the platelet activity (Kerndt & Shivaraj Nagalli, 2023). Even though dipyridamole is not prescribed other than an antiplatelet agent, its other effects include increasing unassisted patency of synthetic arteriovenous hemodialysis grafts (Dixon et al., 2009), inhibiting Mengo virus DNA (Deoxyribonucleic acid) replication (Fata-Hartley & Palmenberg, 2005) and has increased cytotoxic activity against cancer cells compared to normal cells (Afrin et al., 2022) making it a drug repurposing candidate. For a drug's behavior within the patient, half-life, and distribution, and aforementioned affinities, mainly HSA's tendency to accumulate in cancer tissues, the drug interactions with the serum proteins can be crucial in manipulating said properties as well as developing novel therapeutic delivery methods regarding those drugs (Kratz & Elsadek, 2012). The chemical scheme of the drug dipyridamole is given below in Figure 1.4.

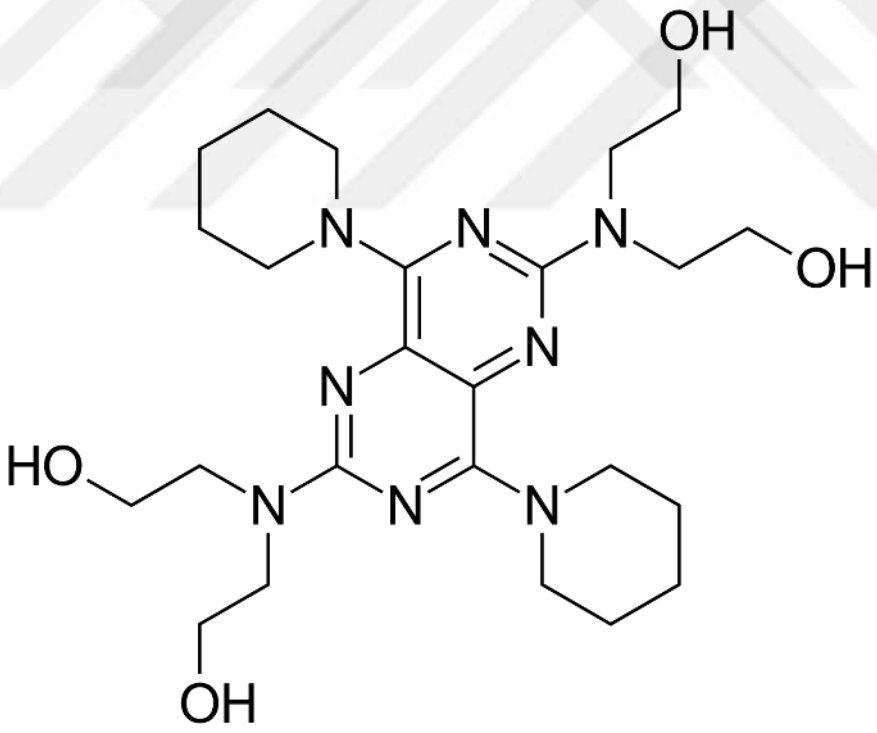

Figure 1.4: Dipyridamole chemical formula

The drug dipyridamole, for its antithrombotic properties, has multiple pathways to achieve such an effect. One is the inhibition of the platelet cAMP-phosphodiesterase.

Following the inhibition the increase in the cAMP content further inhibits platelet activation. Another pathway in which the dipyridamole increases the cAMP content in the resting platelets blocking activation is that the drug inhibits the Equilibrative nucleoside transporter 1 (ENT1) of the red blood cells increasing the adenosine content of the serum. The increased adenosine then activates cAMP production via Adenosine 2A Receptor ($A_{2A}AR$) and Adenosine 2B Receptor ($A_{2B}AR$) activations as presented in the scheme of Figure 1.5 below (Harker & Kadatz, 1983).

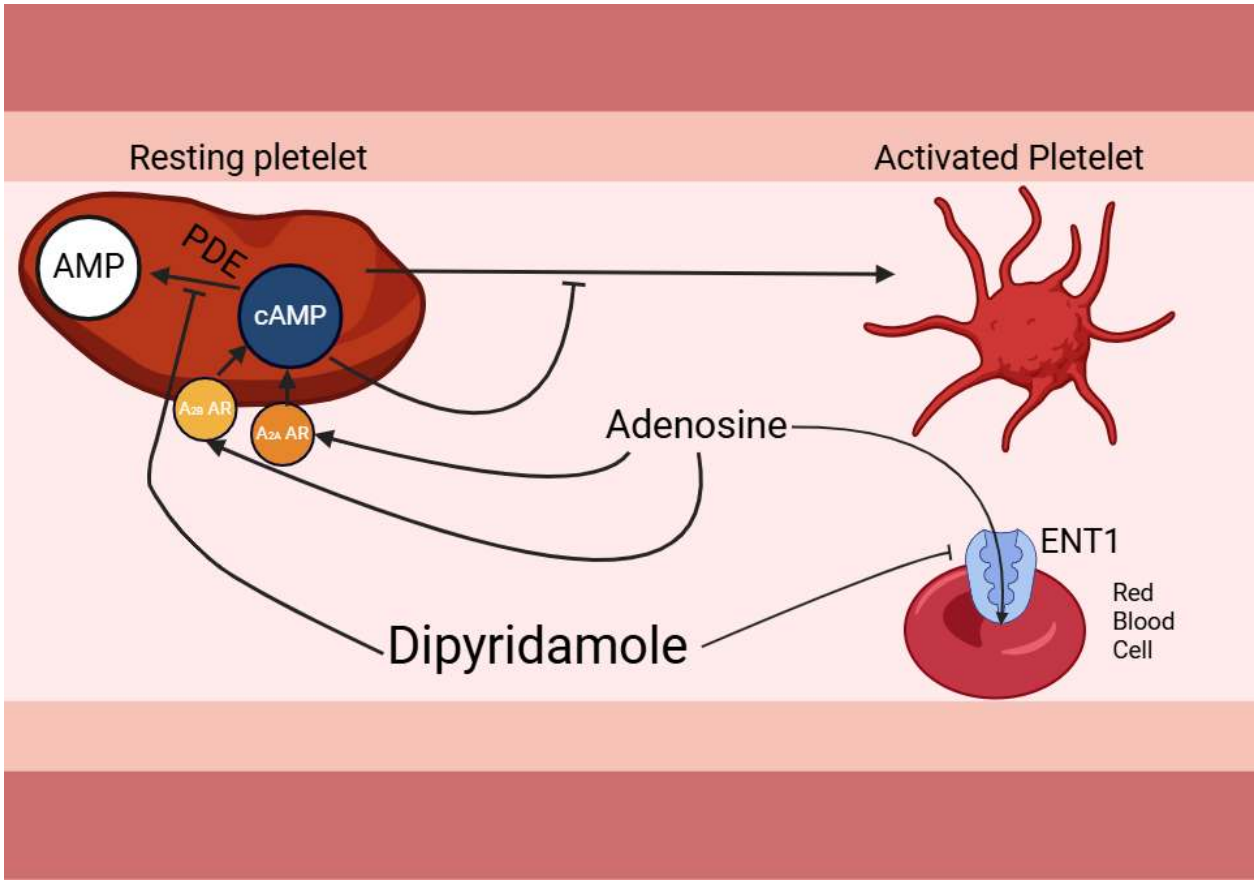

Figure 1.5: The scheme of the operating principle of dipyridamole

1.3 HSA Nanoparticles

Human serum albumin (HSA) nanoparticles are a highly promising trend in the field of nanomedicine, offering a versatile and biologically compatible system for the delivery of therapeutic agents. Derived from HSA, these nanoparticles are typically synthesized

using methods such as desolation, emulsification, or nanoprecipitation. These techniques promote the self-assembly of albumin molecules into nanoscale structures, which can be stabilized through physical interactions or chemical crosslinkers like glutaraldehyde. The resulting nanoparticles possess a uniform size distribution, high surface area, and remarkable stability in physiological environments, making them ideal candidates for systemic administration (Hornok, 2021).

A key advantage of HSA nanoparticles lies in their exceptional biocompatibility and low immunogenicity, as albumin is an endogenous human protein. Furthermore, HSA, as mentioned, possesses multiple binding sites capable of interacting with a wide range of drug molecules, including hydrophobic small molecules, peptides, and drugs. This property enables high drug-loading efficiency and protects the bound agents from premature degradation in lever or clearance in kidneys. Importantly, HSA naturally interacts with cellular receptors such as gp60 and SPARC (secreted protein acidic and rich in cysteine) (Arnold & Brekken, 2009), both of which are overexpressed in many tumor tissues. This allows for receptor-mediated transcytosis and passive accumulation in diseased tissues via the enhanced permeability and retention (EPR) effect, enhancing therapeutic efficacy while minimizing off-target toxicity (Xu et al., 2025).

Beyond oncology, HSA nanoparticles have demonstrated utility in various biomedical applications, including targeted drug delivery, diagnostic imaging, gene therapy, and vaccine delivery. Their long circulatory half-life and capacity for surface modification further enhance their potential, allowing for the conjugation of targeting ligands, imaging agents, or stimuli-responsive elements (Wasko et al., 2024). Overall, HSA nanoparticles represent a robust and adaptable nanocarrier system, with ongoing research continuing to expand their applications in precision medicine and translational therapeutics.

1.4 X-Ray Crystallography

Protein structure determination relies on various techniques, including X-ray crystallography, Nuclear magnetic resonance (NMR) spectroscopy, and electron microscopy. Of these, X-ray crystallography remains one of the most prevalent methods for resolving atomic-level structures of proteins and other biological macromolecules. The process involves crystallizing the target protein, followed by exposure to X-rays. The resulting diffraction patterns are then analyzed to generate electron density maps, which reveal the spatial arrangement of atoms within the molecule (Smyth & Martin, 2000).

An X-ray diffractometer is an essential instrument for determining crystal structures, comprising an X-ray source, a sample holder, and a detector for capturing and analyzing X-ray scattering from crystals. X-ray diffractometer (XRD) is employed to obtain high-resolution diffraction patterns. The atomic arrangement within a crystal scatters X-rays at defined angles, producing characteristic patterns. These patterns are then translated into electron density maps, enabling detailed visualization of the crystal's atomic structure (Bunaciu et al., 2015).

The quality of protein crystals is a critical factor for obtaining high-resolution structures through X-ray crystallography and is influenced by several parameters, including protein purity, concentration, temperature, pH, and the accessibility of the X-ray on the crystals. Protein purity, in particular, plays a significant role in determining crystal order and size (McPherson and Gavira, 2014). To ensure optimal purity, proteins are typically subjected to multiple purification steps using techniques such as affinity chromatography, ion exchange chromatography, and size-exclusion chromatography (Giegé et al., 1995).

The crystallization of a protein occurs after a random collision caused by the nucleation of the protein molecules in the solution and is influenced by the aforementioned factors. The frequency of this event is also related to protein concentration and is differently influenced by each protein. HSA has a biological concentration of 40mg/mL (Tao et al., 2021) hence is inherently resistant to aggregations, requiring higher than usual concentrations for crystallization.

During micro drop crystallography, these higher concentrations may lead to phase separations which are varying size droplets rich in protein separate from the rest of the droplet aqueous solution. These phases may both increase crystal output or decrease it depending on the proteins investigated (Dumetz et al., 2008).

1.5 Common Methods

1.5.1 Gel filtration

Gel filtration or size exclusion chromatography is a column chromatography separating proteins according to their sizes. The mobile phase is often an aqueous buffer depending on the stability requirements of the protein and the stationary phase is a porous matrix that entraps and retards the larger proteins up to a limit determined by the pore sizes in the stationary matrix (Ó'Fágáin et al., 2010). When using gel filtration for buffer exchange purposes first the column is equilibrated with the final buffer, when the sample is loaded, the smaller the molecule the later it arrives at the fractions hence the largest molecules, the proteins, arrive earlier than the chemical components of the initial sample (Thermo Fisher Scientific Inc., 2025).

1.5.2 SDS-Page gel electrophoresis

Sodium dodecyl sulfate-polyacrylamide gel electrophoresis (SDS-PAGE) is a widely employed technique for visualizing proteins in a sample based on their molecular weights. In this method, proteins are first denatured by the anionic detergent SDS, which disrupts

non-covalent bonds and imparts a uniform negative charge proportional to the length of each polypeptide chain. Reducing agents such as β-mercaptoethanol/2-mercaptoethanol (BME) or dithiothreitol (DTT) are commonly included to cleave disulfide bonds. Depending on the viscosity of the sample it is optional to heat-treat the samples for more efficient denaturation. Once treated, the protein samples are loaded onto a polyacrylamide gel composed of a stacking gel (low acrylamide concentration, pH ~6.8) and a resolving gel (higher acrylamide concentration, pH ~8.8), which together enhance band resolution during electrophoresis (Archuleta, 2024) The protein loading wells have a significant size when compared to the total length of the gel hence the stacking gel ensures the entire protein content of the sample is in close proximity when they enter the separating gel.

Upon application of an electric field, the SDS-coated proteins migrate through the gel matrix toward the anode, with smaller proteins traversing the gel more rapidly than larger ones due to the pore sizes constraining the larger proteins. This results in a size-dependent separation of proteins in bands. Following electrophoresis, proteins are visualized using staining methods such as Coomassie Brilliant Blue or silver staining. The inclusion of a molecular weight marker or protein ladder enables the determination of protein sizes in the samples. Overall, SDS-PAGE remains a fundamental tool in protein analysis(Al-Tubuly, 2000).

1.5.3 Column Chromatography

Column chromatography is a commonly used separation technique in biochemistry and analytical chemistry to isolate individual components from complex mixtures based on their differential affinities for a stationary phase and a mobile phase. In this method, the mixture to be separated is applied to the top of a column packed with a stationary phase,

typically composed of silica gel, alumina, or various types of resins, depending on the specific affinity of separation chosen. A solvent or a series of solvents, known as the mobile phase or eluent, is then passed through the column, allowing the sample components to migrate at different rates according to their polarity, size, charge, or specific binding interactions with the stationary matrix (Srivastava et al., 2021).

The elution behavior of each component in the sample mixture is determined by its physicochemical properties and its relative interaction with the stationary and mobile phases. Less strongly retained molecules elute first, while those with stronger interactions move more slowly and elute later. Fractions collected from the column can then be analyzed individually, enabling the identification, purification, or quantification of specific compounds. Column chromatography is highly versatile, encompassing various modes such as ion exchange chromatography, size exclusion chromatography (SEC), affinity chromatography, and reverse-phase chromatography, each tailored to particular molecular characteristics. This technique remains indispensable in both preparative and analytical workflows, particularly in protein purification, metabolite separation, and compound isolation (Kumari et al., 2022).

Chapter 2

MATERIALS AND METHODS

2.1 Materials and equipment

2.1.1 Buffer solutions

The buffers and solutions used in these experimentations are provided below as tables in Table 2.1, Table 2.2, and Table 2.3

Table 2.1: NaOH cleaning solution recipe.

Reagent	Final Concentration	Amount
NaOH	**0.1 M**	**0.4 g**
ddH_2O		**1 L**
Total		**1 L**

Table 2.2: SEC Buffer recipe.

Reagent	Final Concentration	Amount
NaCl	**150 mM**	**8.766 g**
Tris	**20 mM**	**6.06 g**
ddH_2O		**Up to 1 L**
Total		**1 L**

Table 2.3: Sec buffer with 2-mercaptoethanol (BME) recipe

Reagent	Final Concentration	Amount
NaCl	**150 mM**	**8.766 g**
Tris	**20 mM**	**6.06 g**
BME	**5.72 mM**	**0.4 mL**
ddH_2O		**Up to 1 L**
Total		**1 L**

2.2 Purification of HSA

The HSA used was commercially available intravenously administered medicine Albuman™ by Centurion brand (200mg/mL). Size exclusion chromatography was performed on an AKTA-Go FPLC device. A Superdex™ 200 column was attached to the AKTA-Go and equilibrated with SEC buffer (refer to Table x) until the UV absorbance was stable. A total of 1 ml of HSA solution was manually injected using a 5 ml loop in the manual load mode of the AKTA-go system. Afterward, the system was switched to inject mode. After a 10-minute waiting period, the system was changed back to manual load mode. Using the fraction collector of the instrument, all of the fractions were collected in a 15 ml falcon tube. This size exclusion was done for the purposes of buffer exchange. The contents of the fractions were tested in SDS-Page gel electrophoresis Using Amicon concentrators the pure protein was concentrated up to 99 mg/mL, this final concentration was confirmed using a nanodrop spectrophotometer. The protein was then added to the drug dipyridamole until its solubility limit (with the undissolved drug visible) and stored in a +4°C fridge. Figure 4 gives a simplified summary of the HSA purification and crystallization. To ensure the reliability of the data, the sec column is washed with 0.1M NaOH buffer from Table 2.1 before and after adding the sample.

2.3 SDS-Page gel electrophoresis

The concentrated pure HSA samples were run through 15% SDS-Page gels using a homemade ladder and dye, The loaded samples were run at 90V for half an hour and then at 120V for an hour, then soaked in dye for half an hour before being destained overnight.

2.4 Crystallization of HSA

The protein sample was mixed with over 3000 crystallization solutions in the Kuybiig-M (Koç University Structural Biology and Innovative Drug Design Center) library in equal

volume (0.83µL to 0.83µL) and covered with a 16.6µL of paraffin oil. Among all those the protein crystallized in commercial crystallization solution crystal structure #39 consisting of 2.0M Ammonium Phosphate Monobasic in 0.1M Tris 8.5 pH solution. The crystals were first observed after three weeks of room temperature incubation in the Terasaki plate in a dark environment.

2.5 Data collection

Ambient temperature X-ray crystallographic data was collected using Rigaku's XtaLAB Synergy

R Flow XRD system according to the Turkish DeLight X-ray source protocols (Gül et al., 2023) found in the University of Health Sciences, Istanbul, Türkiye. Multiple crystals were screened using the modified adapter of the XtalCheck-S plate reader. During the data collection due to protein precipitation, the crystals were not visible yet upon searching in the well multiple areas gave x-ray diffraction data. The duration of exposure time was optimized to minimize the potential radiation damage caused by X-rays. Diffraction data were collected on different days for a total of approximately 10 hours. The detector distance was set at 100.0 mm, and the scan width and the angle of the plate were arranged to cover around 80°.

2.6 Data processing

The diffraction data were set up in CrysAlisPro to complete the automated data reduction. The collected data was then merged using the profit merge process with CrysAlisPro 1.171.42.59a software (Rigaku OxfordDiffraction, 2022) to produce an integrated reflection dataset (*.mtz) file for further analysis (Mehmet Gül et al., 2023). As the photon scattering results create images, all reflection images were investigated within the software with peak search followed by determining the unit cell. The frames with the same unit cells and space groups were merged via a script created by the "xx proffitbatch" command

within the software. The merging of the reduced data was then outputted as a .mtz map file.

The Phenix software was used for molecular replacement and refinement. The .mtz file was first investigated by Xtriage within PHENIX to confirm the quality of the map and then PHASER-MR was used for molecular replacement. (Adams et al., 2010). The molecular replacement used a previously published HSA crystal (PBD ID: 1AO6) was used. The molecular replacement was used for molecular replacement and refinement to fully position the folded protein chains into the three-dimensional electron map of the .mtz file. The resulting .pdb protein structure file was then manually constructed in Coot version 0.9 (Emsley and Cowtan, 2004) and further refined in PHENIX

2.7 Pisa and Other Statistical Analyses

The bond lengths, counts, and interface surface areas were calculated and generated using PDBePISA online software (Krissinel & Henrick, 2007). All deposited PDB unique HSA structures (excluding non-crystal structures and ones with non-HSA peptides) were put through the PDBePISA and then their given interface surface areas, bond quantities, and space groups were collected in a Microsoft Excel file, and the histogram figures were constructed using the Microsoft Excel software.

2.8 Figure and Table Generations

The figures were generated using Bio Render software and the tables were made using Microsoft Excel software. Figures 3.9-3.17 were prepared using the Pymol visualization tool.

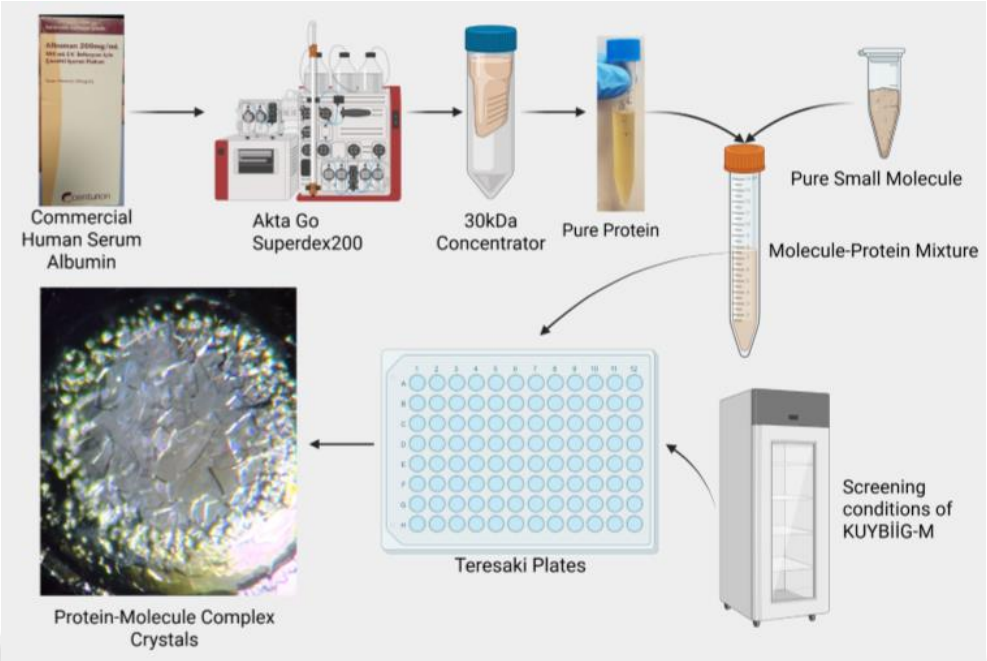

Figure 2.1: Flowchart of Crystallization

2.9 Molecular Docking

Molecular docking calculations were performed using Autodock 4.2 software by Scripps Research Institute. The PDB structure of HSA protein with a resolution of 2.50Å complexed with warfarin was downloaded from the protein data bank. (PDB ID: 1H9Z) (Ghuman et al., 2005). Protein preparation was done by removing water molecules, protonating the polar atoms, and adding Kollman charges. The active site and the grid box (30 × 30 × 30 Å, 0.4 Å spacing) of the protein were selected as the center of the warfarin (x = -8.477, y = -8.007, z = 8.904) present in the crystal structure. Finally, the dipyridamole molecule was modeled and minimized by the MMFF94s forcefield in Avogadro software (Hanwell et al., 2012) and prepared in Autodock. After ligand preparation, dipyridamole was docked into the active site that had been designated previously. Discovery Studio Visualizer (BIOVIA, 2023) software was used to analyze the docking results.

Chapter 3

RESULTS

3.1 Purification of HSA via Gel Filtration

The Human Serum Albumin source of the experiment was a commercially sold intravenously administered drug named Albuman™ from the Centurion brand. Initial crystallization attempts using the protein directly did not yield protein crystals hence a further purification step was added to the workflow to eliminate the protective and stabilizing agents in the drug mixture (Porath & Flodin, 1987). The large-scale chromatogram of this gel filtration is presented below in Figure 3.1.

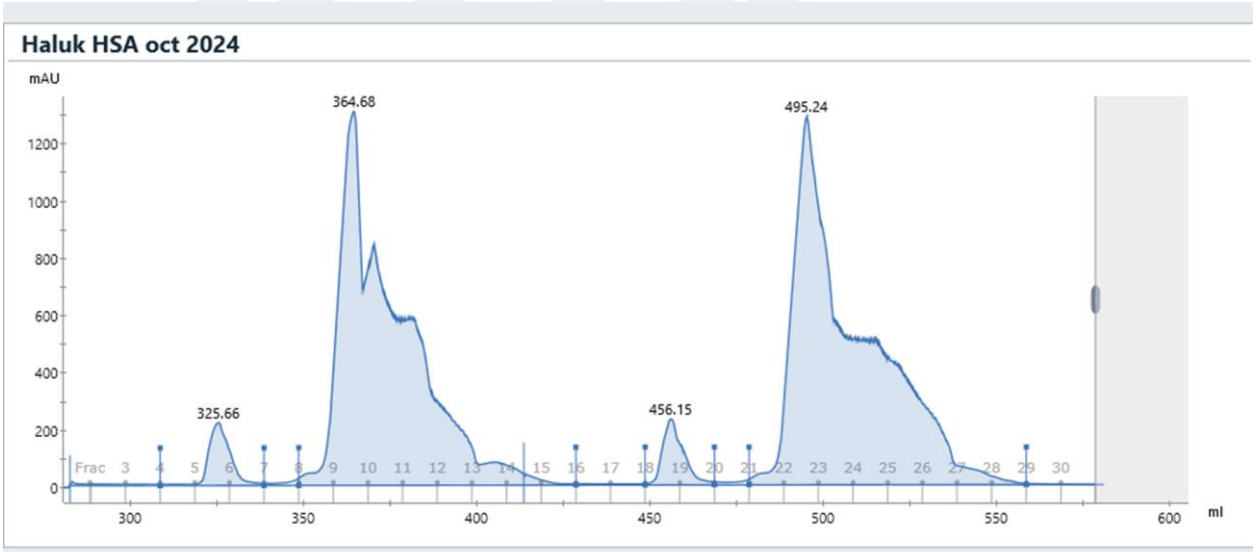

Peak Table - UV

Peak	Retention ml	Area mlmAU	Area %	Ext coeff. mg⁻¹ ml cm⁻¹	Fraction(s)	Volume ml	Conductivity mS/cm
Peak A	325.659	1543	2.77		4 - 6	29.997	17.38
Peak B	364.681	25170	45.14		8 - 15	80.005	17.13
Peak C	456.153	1561	2.8		18 - 19	19.998	17.36
Peak D	495.238	27484	49.29		21 - 28	80.005	17.11

Figure 3.1: Large-scale HSA purification chromatogram

As the chromatogram had shown a small peak and a large peak with a shoulder, from the same Albuman^{TM} bottle much less sample, (0.4uL) was loaded to confirm the bottle's content without BME in Figure 3.2 and with BME in Figure 3.3.

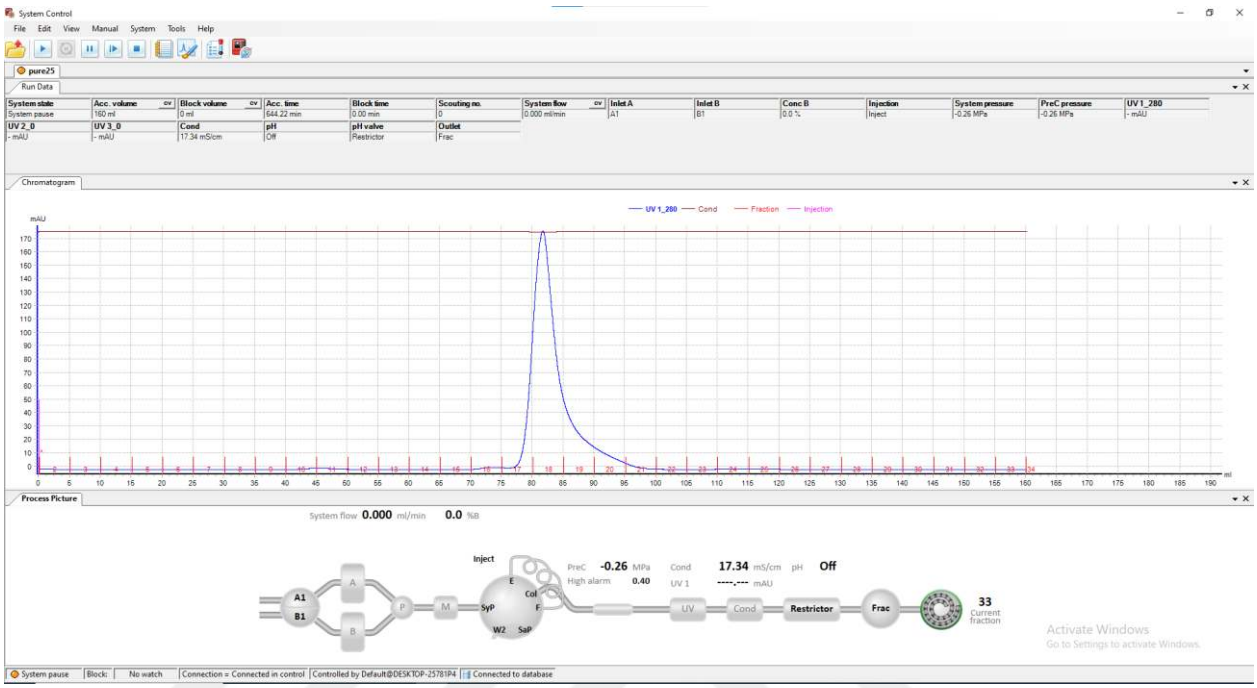

Figure 3.2: Small-scale HSA purification chromatogram

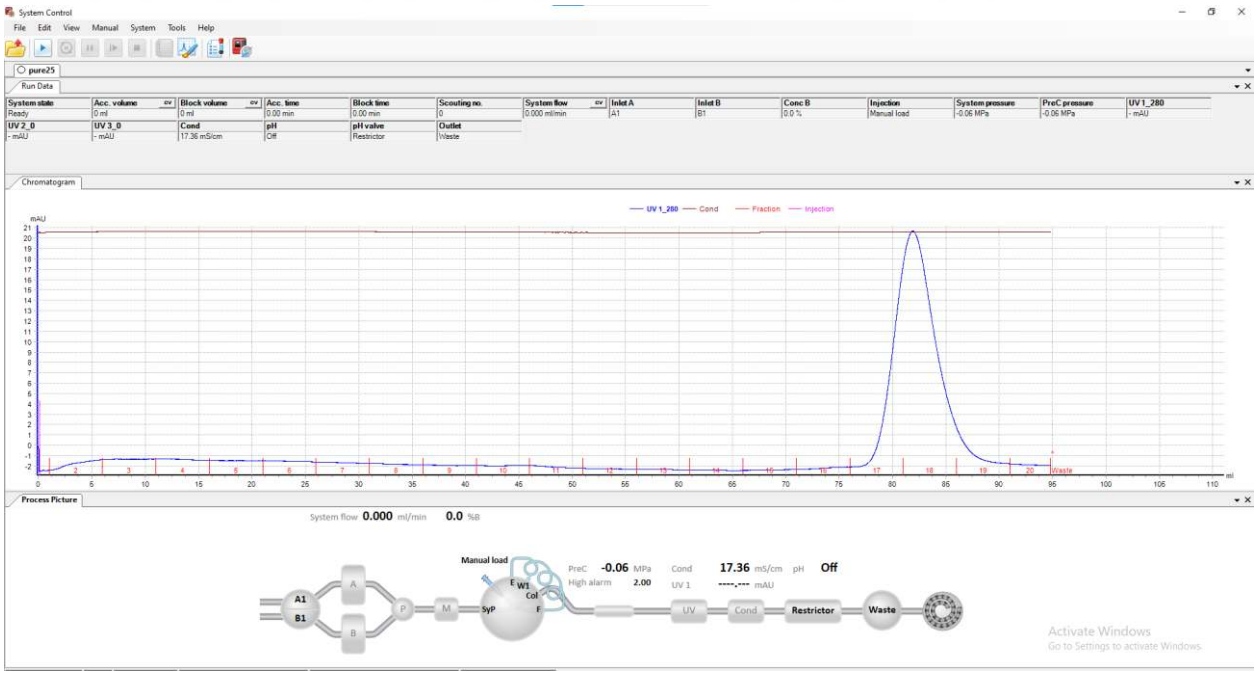

Figure 3.3: Small-scale HSA purification with BME chromatogram

The low-concentration loading trial showing a single peak confirms the shoulder in the initial gel filtration was an outlier result caused by either equipment or user error. The fractions were then concentrated using 30.000Da and 10.000Da amicon concentrators. At the end of each 2 mL purification, approximately 3 mL of 100 mg/mL protein solution was acquired and crystallized. The concentrated, dipyridamole-added protein mixtures were stored in a +4°C fridge.

3.2 Purity confirmation of HSA via SDS-Page gel electrophoresis

After the gel filtration, for protein content confirmation SDS-Page electrophoresis was performed, even though the unintended overload present in Figure 3.4, the sample being without any other proteins is understandable. For better visualization, Figure 3.5 is the combination and pairing of Figure 3.1 and Figure 3.4. According to Figure 3.5, the first small peak even though is UV-reactive, does not include proteins.

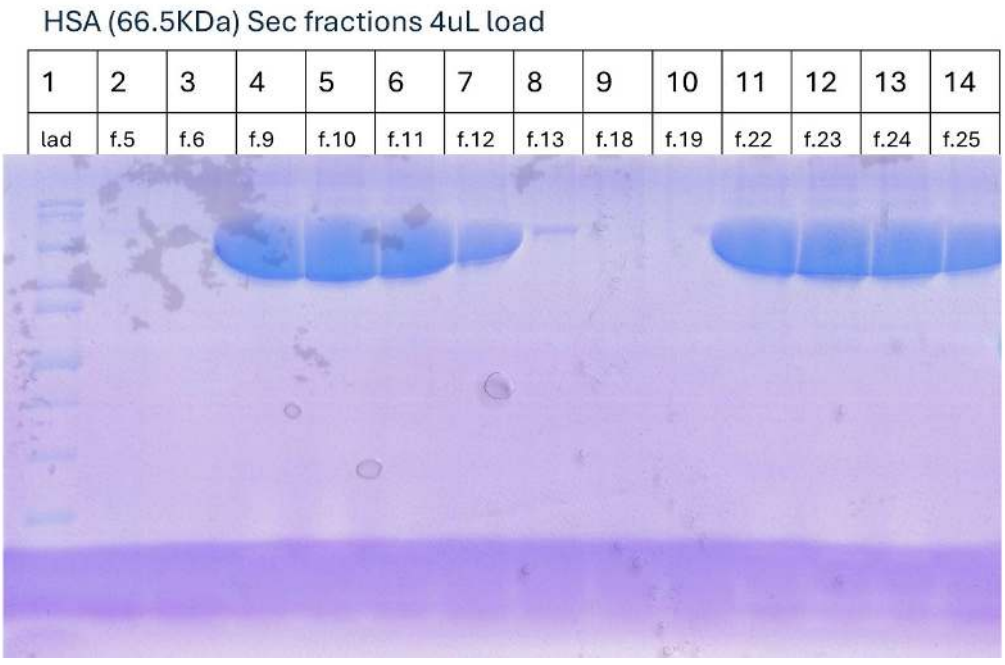

Figure 3.4: The SDS-Page gel results of the large-scale HSA purification.

For easier visualization, the chromatogram and the gel are combined in the same image with fraction/column pairings visualized with arrows.

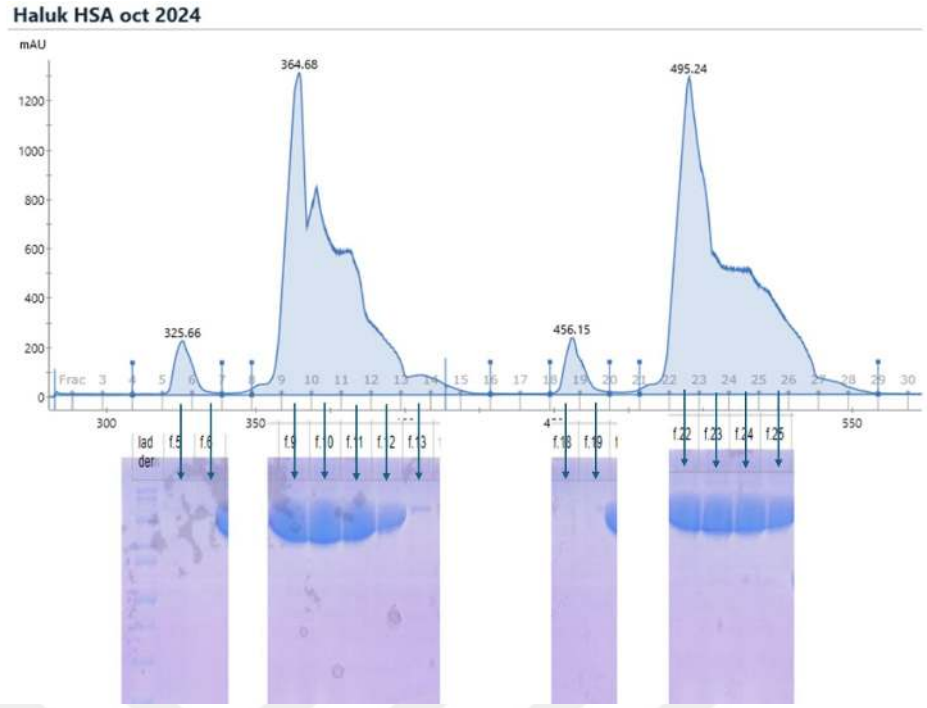

Figure 3.5: The paired HSA purification and SDS-Page gel results

3.3 Crystallization Outcomes

The drug dipyridamole was directly added to the concentrated protein and incubated overnight at +4°C, the drug was added until there was a visible undissolved drug in the tube making the dipyridamole content its solubility limit in water-based solutions. The mixtures were then tested using approximately 3500 unique crystallization conditions in sitting drop vapor diffusion crystallization procedures. Different trials used different protein concentrations 200 mg/mL vs. 150 mg/mL vs. 100 mg/mL) incubated in different temperatures (+4°C vs. +22°C).

The crystals were then tested in Rigaku's XtaLAB Synergy R Flow XRD system according to the Turkish DeLight X-ray source and differentiated as salt crystal vs. protein crystal. The first HSA protein crystals observed were in the condition mixture wizard IV #21 consisting of 0.83 μL 25% (w/v) polyethylene glycol (PEG) 2500, 100mM PCB pH 5.00 buffer mixed with equal volume 200 mg/mL HSA in Sec buffer (table 2.1) covered with 16.6 μL paraffin oil. The initial observation of the crystals was clear as seen in Figure 3.6

below, yet in a few days up to the X-ray diffractometer visit discolored phase separations had covered the crystals as provided in Figure 3.7 below.

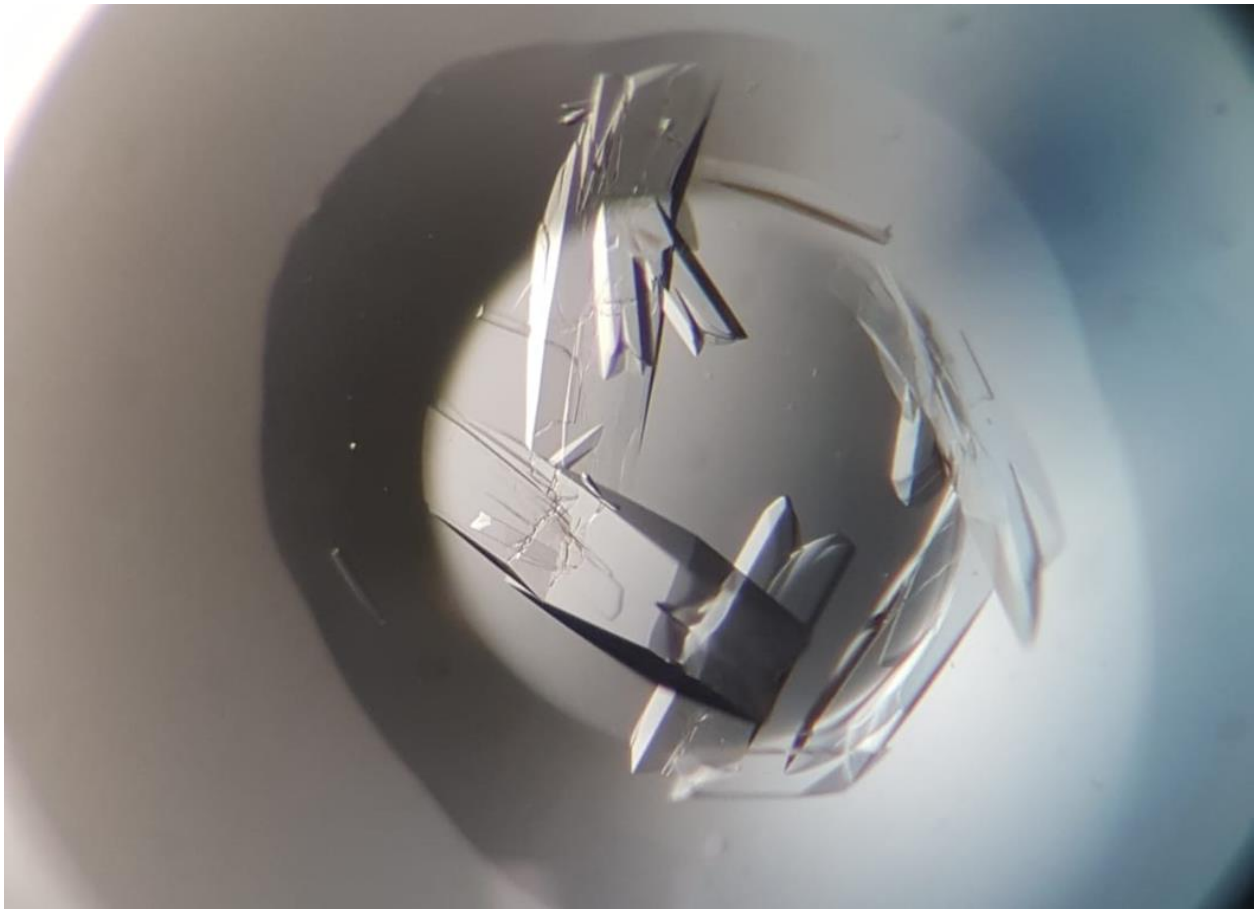

Figure 3.6: The initial state of the first crystal.

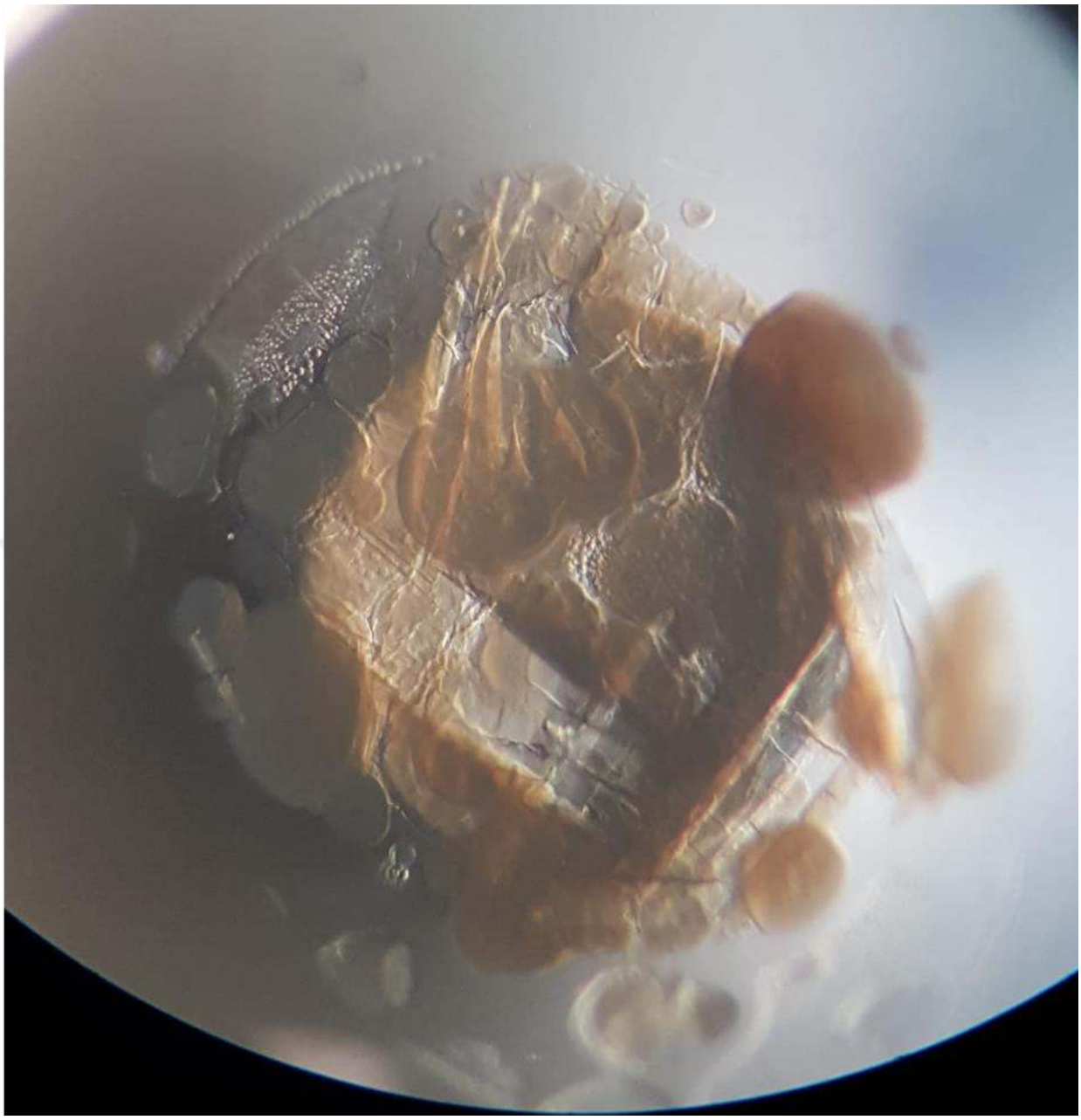

Figure 3.7: The state of the first crystal during ambient data collection.

The diffraction data collected suggesting this is a protein crystal is also given below in Figure 3.8. The data collected was not sufficient to solve the structure and although numerous 72-well Terasaki plates were set up using the same conditions in the same temperature incubations the replicates of these crystals were not observed.

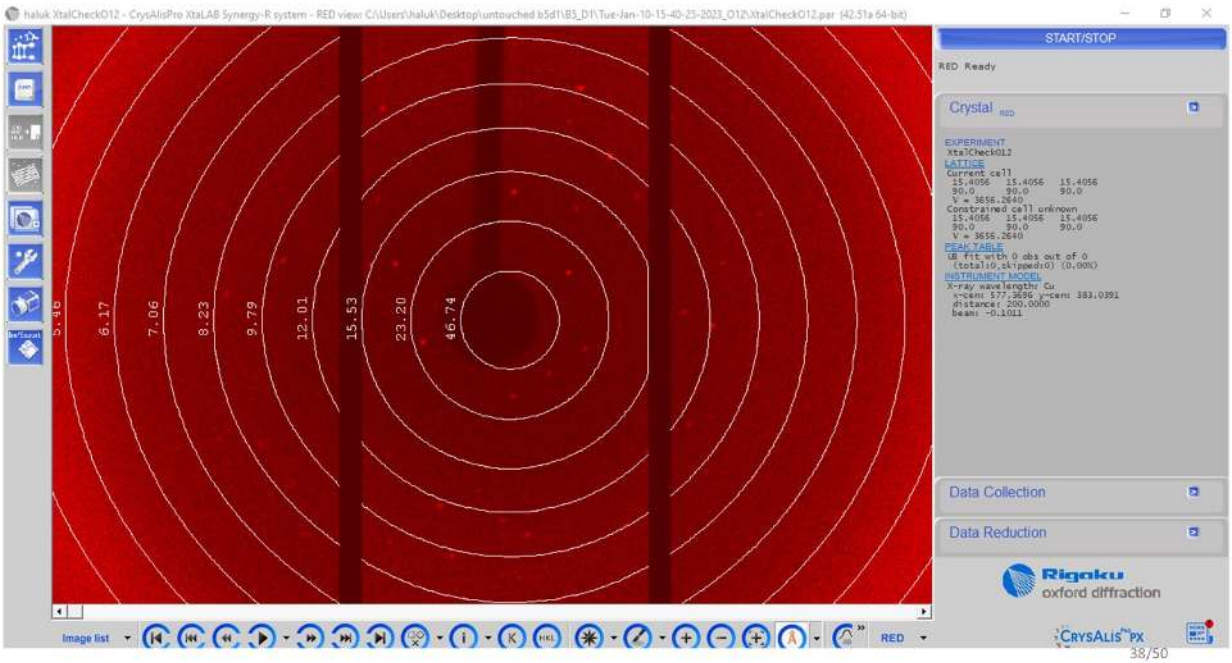

Figure 3.8: The ambient data collected from the first crystal.

Those crystals were also picked using loops for cryogenic data collection, collection provided below, however, the data was still not enough for solving the structure.

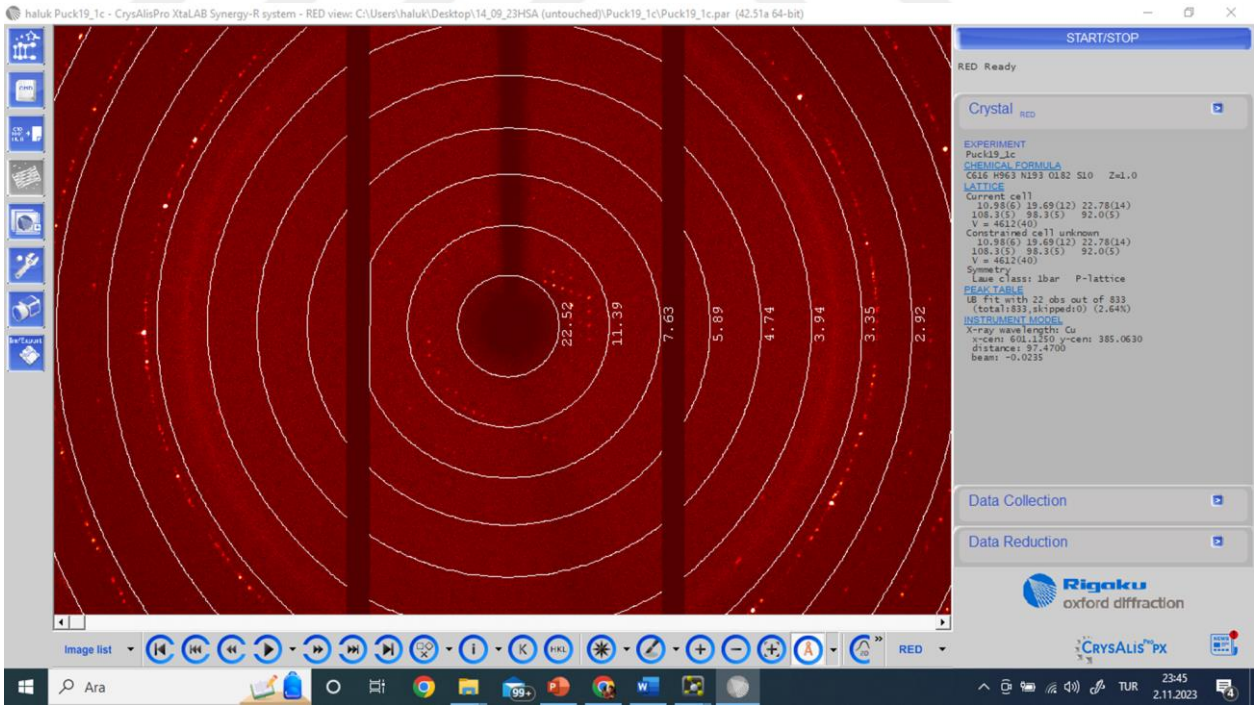

Figure 3.9: The cryogenic data collected from the first crystal.

The second wave of crystals was acquired in the mixture with 0.83 μL crystal structure I # 39 consisting of 2.0M ammonium phosphate monobasic with 0.1M tris pH 8.5 buffer

solution mixed with 0.83 μL protein solution of 100 mg/mL protein concentration, 150 mM NaCl and 20 mM Tris pH 7.35, covered in 16.6 μL paraffin oil. The images of these crystals are given below in Figure 3.10.

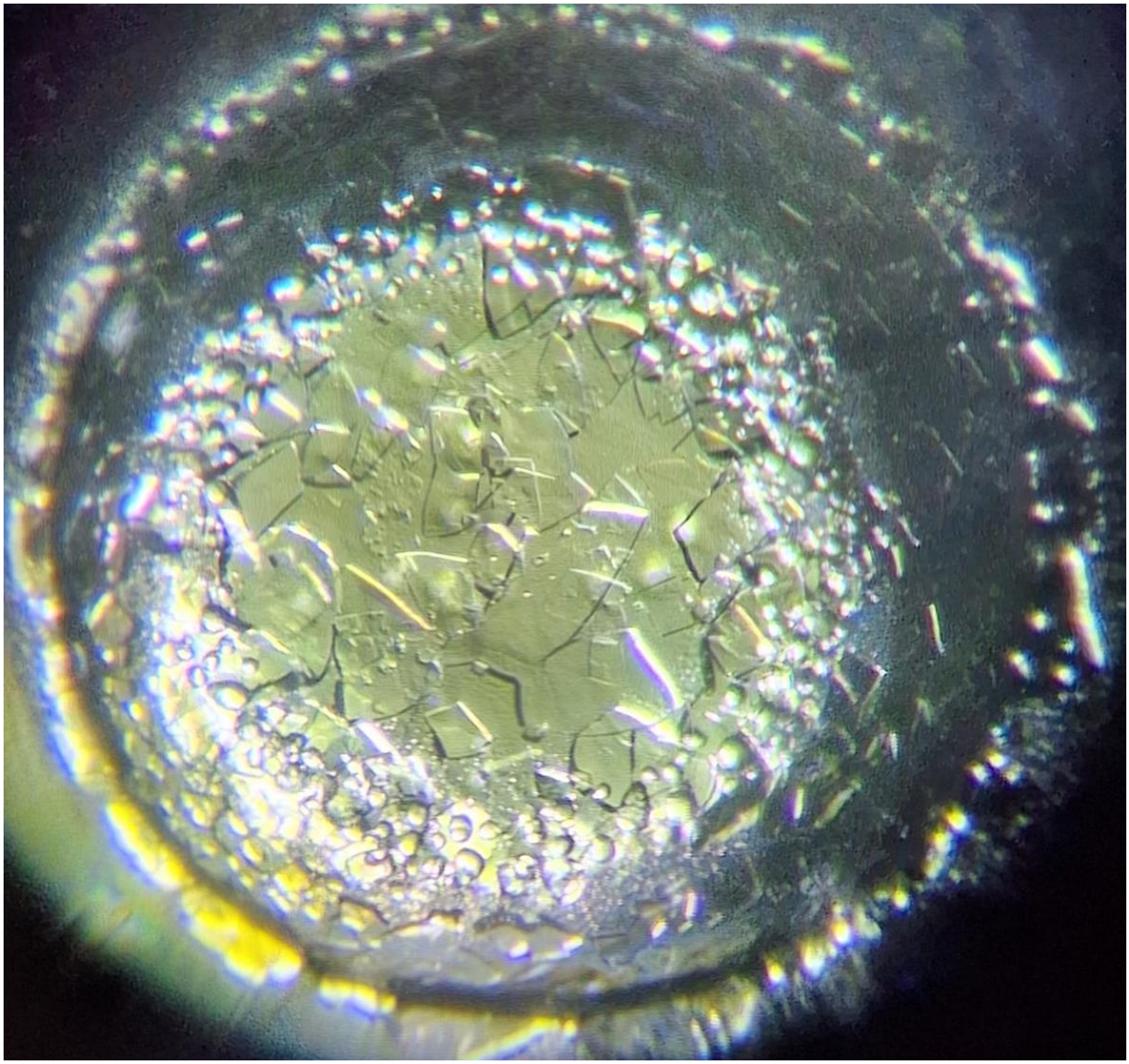

Figure 3.10: The second crystals.

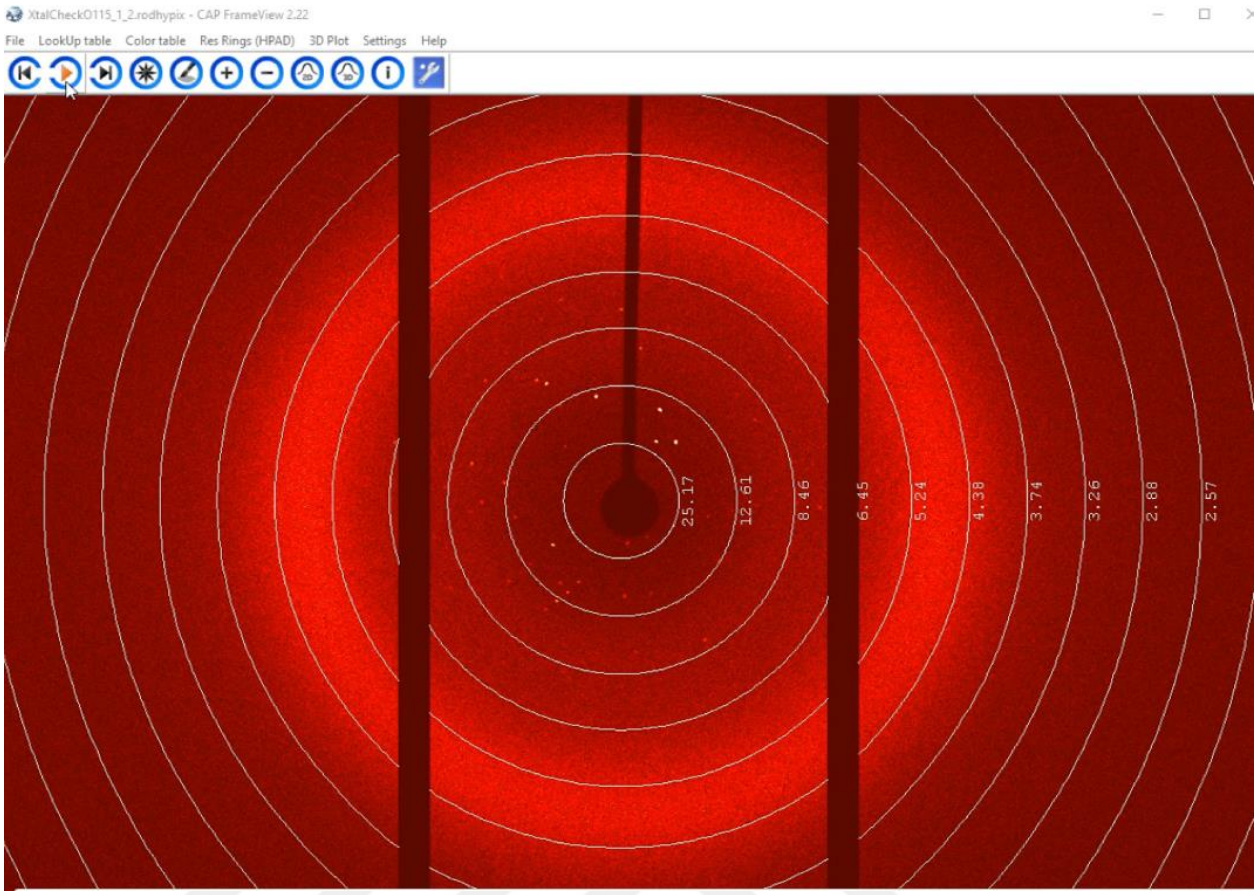

Figure 3.11: Data collected from the second crystals.

Data collected from these crystals were enough to construct the structure of the protein, however, replicates of these conditions were also set up for future experiments with again no new crystals being observed.

3.4 Data processing

The data collected was first analyzed in the crysalispro software and was merged into a .mtz file named “overthingmerged”. The data has a relatively high resolution (2.50 Å) and high completeness (94.9%) as given in Table 3.1. The parameters of the refinement cycles are presented in Table 3.2

Table 3.1: The CrysAlisPro data merging results of the second crystals.

resolution (A)	# kept	# theory	# unique	complete	average redundancy	mean F2	mean F2/sig(F2	Rint	SigmaB	CC 1/2	CC*	deltacc	Rurim	Rpim
29.41- 6.22	91300	4707	4514	95.9	20.2	27.92	16.47	0.223	0.071	0.988	0.997	0.0234	0.232	0.048
6.22- 4.92	95057	4707	4642	98.6	20.5	13.09	6.42	0.511	0.187	0.912	0.977	0.0179	0.617	0.11
4.92- 4.29	97962	4707	4643	98.6	21.1	16.55	6.84	0.511	0.184	0.904	0.974	0.0173	0.608	0.108
4.29- 3.90	96487	4707	4644	98.7	20.8	10.92	5.06	0.59	0.238	0.876	0.966	0.0154	0.793	0.126
3.90- 3.62	87966	4707	4612	98	19.1	6.94	3.82	0.676	0.323	0.82	0.949	0.0114	1.083	0.153
3.62- 3.40	81336	4707	4560	96.9	17.8	4.64	2.69	0.768	0.432	0.698	0.907	0.0027	1.518	0.182
3.40- 3.23	75766	4707	4478	95.1	16.9	3.18	1.9	0.839	0.559	0.617	0.873	-0.0032	2.087	0.204
3.23- 3.09	71900	4707	4454	94.6	16.1	2.29	1.28	0.894	0.664	0.536	0.835	-0.0089	2.884	0.223
3.09- 2.97	70422	4707	4444	94.4	15.8	1.68	0.92	0.925	0.726	0.529	0.832	-0.0094	4.068	0.233
2.97- 2.86	66924	4707	4409	93.7	15.2	1.47	0.77	0.936	0.762	0.515	0.824	-0.0104	4.655	0.24
2.86- 2.77	63868	4707	4412	93.7	14.5	1.27	0.65	0.948	0.782	0.508	0.821	-0.011	5.614	0.25
2.77- 2.70	62002	4707	4372	92.9	14.2	1.08	0.5	0.953	0.799	0.515	0.824	-0.0104	6.455	0.253
2.70- 2.62	59890	4707	4300	91.4	13.9	0.85	0.41	0.955	0.834	0.519	0.826	-0.0102	8.671	0.255
2.62- 2.56	58730	4707	4286	91.1	13.7	0.76	0.37	0.961	0.852	0.477	0.804	-0.0131	11.92	0.26
2.56- 2.50	56234	4710	4249	90.2	13.2	0.75	0.33	0.959	0.848	0.502	0.818	-0.0114	9.942	0.263
29.41- 2.50	1135844	70608	67019	94.9	16.9	7.36	3.8	0.62	0.352	0.919	0.979	0.661	1.184	0.147

Table 3.2: The data quality table after refinement.

PDB ID	N/A		
Data collection	HSA	Rwork / Rfree	0.254/0.320
X-ray source	Turkish DeLight	**No. atoms**	
Temperature (K)	298	Protein	13599
Space Group	I 1 2 1	Ligand / Ion / Water	348
a,b,c (A˚)	87.80, 116,49, 205,46	***B*** **-factors**	
α,β,γ (°)	89.9, 99.25, 90.02	Protein	
Resolution	29.41-2.50	Ligand / Ion /Water	
CC1/2	0.919	Coordinate errors	0.61
*CC**	0.979	Bond lengths (˚A)	0.010
I/σI	3.8	Bond angles (°)	1.332
Completeness (%)	94.9	**Ramachandran plot**	
Refinement		Favored (%)	95.2
Resolution	2.5˚A	Allowed (%)	4.5

No. reflections	61139	Disallowed (%)	0.30

3.5 Structural Analyses

The structure is submitted to the PDB Database with the given accession code “9V61” It can be understood from Figure 3.12 that the space-filling of the repeating unit has two distinct dimerization patterns, first being between chains A and B colored blue and green in Figure 3.14.b and the other being where two asymmetric units interlock into each other between their chain C’s. The alignment of the chains of the structure is presented in Figure 3.13.

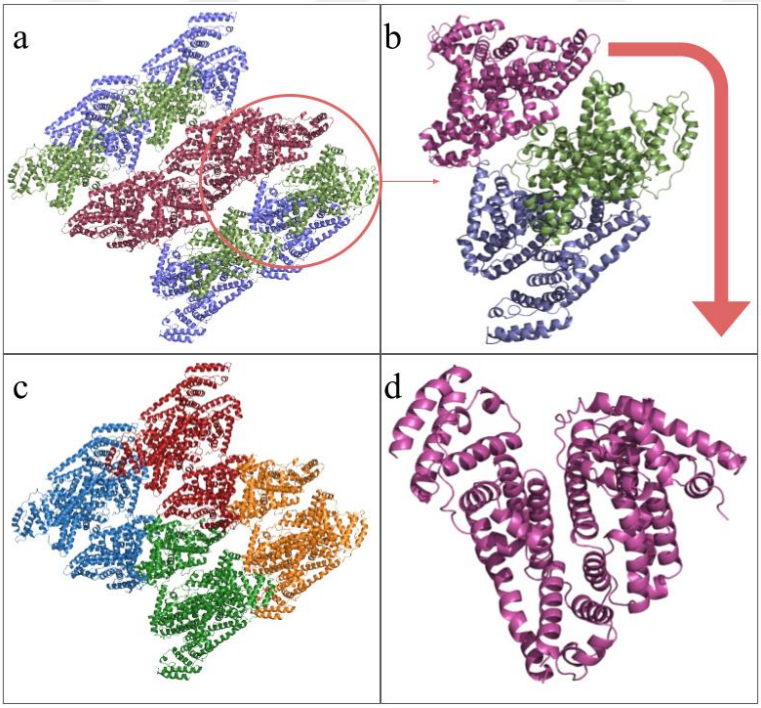

Figure 3.12: The visualization of the crystal packing and asymmetric unit. (a) The repeating unit of the solved structures consists of 4 asymmetric units each containing three HSA proteins. Colored by chains in the asymmetric unit (b) A Single asymmetric unit consisting of three individual protein chains is extracted from the repeating unit. (c) The repeating unit with individual asymmetric units is colored differently. (d) Single HSA protein (Chain C) extracted from the asymmetric unit.

The solved structure is presented in Figure 3.12. How the asymmetric unit assembles to the repeating unit is presented as a flowchart, the entire repeating unit filling the *I 1 2 1* space is presented in Figure 3.12a with all unique protein chains colored individually. The single asymmetric unit is extracted into Figure 3.12.b. The repeating unit consists of four asymmetric units as seen in Figure 3.12c with each asymmetric unit consisting of three protein chains colored differently. A single HSA chain is shown in Figure 3.12d.

Figure 3.13a and Figure 3.13b focus on slight differences between the unique chains in the asymmetric unit while Figure 3.13c and Figure 3.13d offer front and back views of the total alignment structure. The alignment was done by perfectly fitting the longest alpha helixes of the chains, residues between 365 and 398. Root mean square deviation (RMSD) values between the different chains are A-B 0.461, A-C 0.522, and B-C 0.625 presented by pymol alignment tools. The overall structure of these dimers in relation to each other is presented in Figure 3.13, and individual independent visualizations of these dimers are presented in Figure 3.14. The differences were enough to consider them different chains in a large asymmetric unit cell rather than symmetries of a single chain. The differences are also concentrated in the disordered links between the helixes while the helixes which are often kept stable via disulfate bonds are overlapping. This also suggests that these HSA-HSA interactions do not alter the main shape of the proteins.

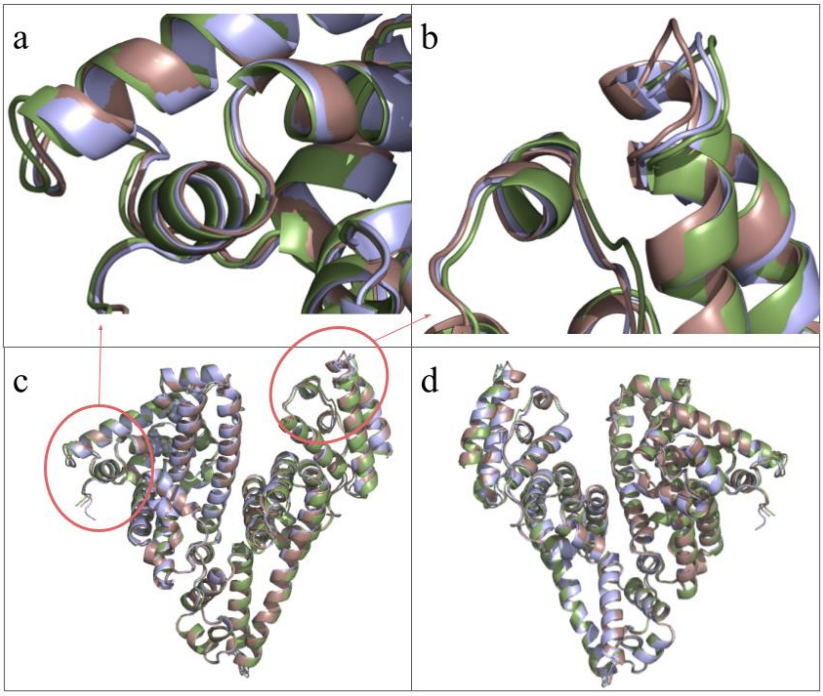

Figure 3.13: The alignment of the three separate chains in the asymmetric unit. Chain is colored green B and chain C is colored brown. (a) This panel focuses on the slight shift between the helices of Ia-H3 and Ia-H4. (b) This panel focuses on the slight shift between the helices of IIIb-H3 and IIIb-H4. (c) This panel shows the overall alignment from the front. (d) overall alignment from back

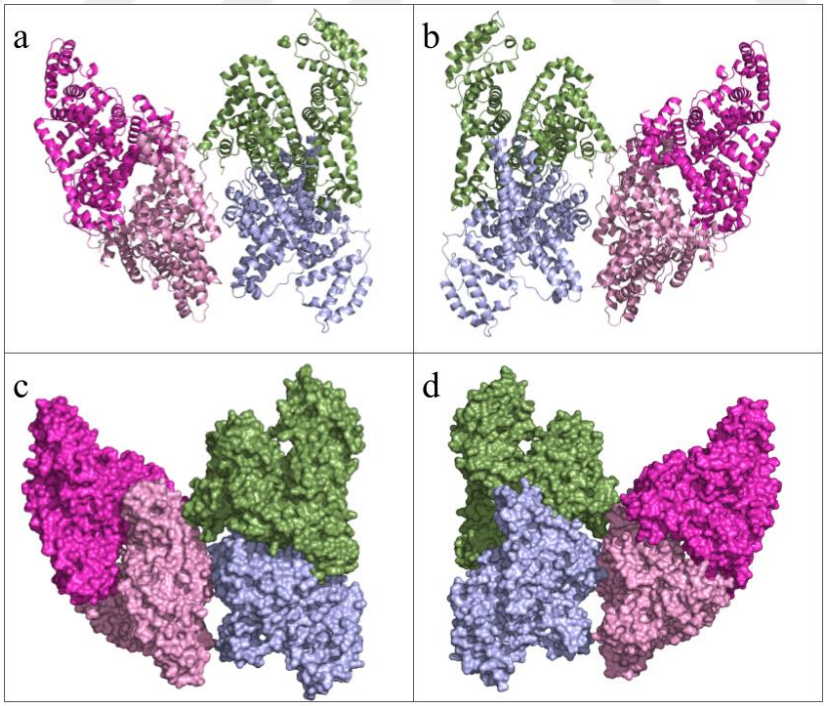

Figure 3.14: The two distinct dimers presented. Chain A is colored blue, Chain B is colored green, Chain C is colored light pink and the other asymmetric unit's chain C is colored in magenta. (a) Four albumins are arranged in two distinct dimer formations in cartoon representation, front view. (b) Four albumins are arranged in two distinct dimer formations in cartoon representation, back view. (c) Four albumins are

arranged in two distinct dimer formations in surface representation, front view. (d) Four albumins are arranged in two distinct dimer formations in surface representation, back view.

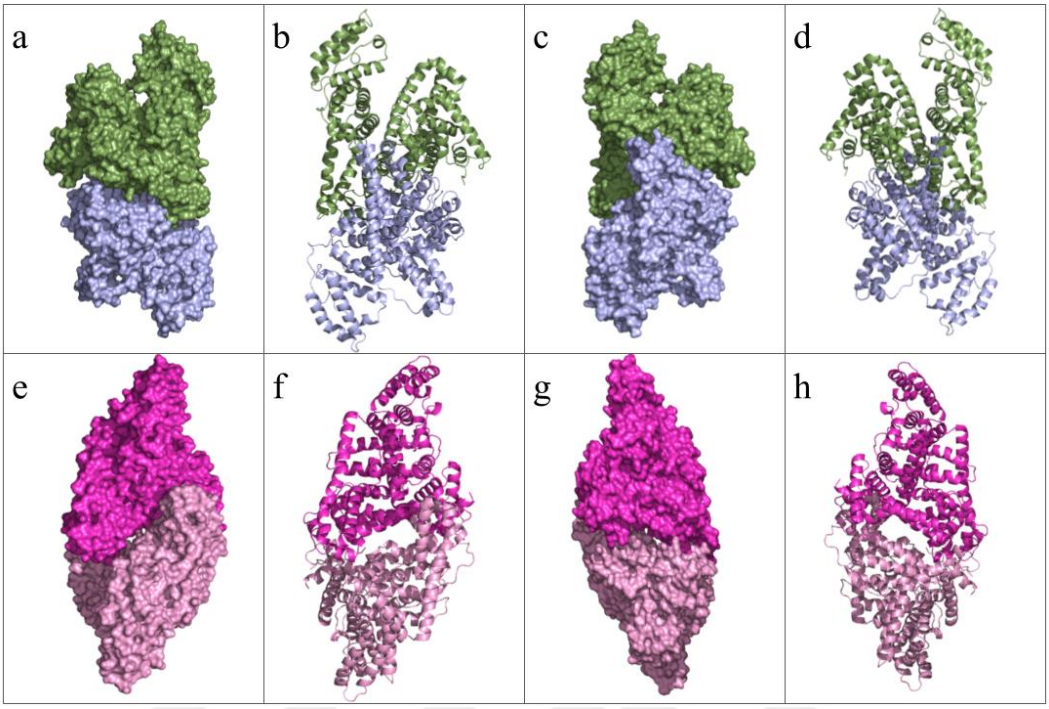

Figure 3.15: The two dimerized structures are visualized separately, as cartoons and surfaces. Chain A is colorized blue, Chain B is colorized green, Chain C is colorized light pink and the other asymmetric unit's chain C is colorized in magenta. (a) The dimer of the chains A and B, shown in the front view as surfaces. (b) The dimer of the chains A and B, are shown in front view as cartoons. (a) The dimer of the chains A and B, shown in the back view as surfaces. (b) The dimer of the chains A and B, are shown in the back view as cartoons. (e) The dimer of the chains C1 and C2, shown in the front view as surfaces. (f) The dimer of the chains C1 and C2, shown in the front view as cartoons. (g) The dimer of the chains C1 and C2, shown in the back view as surfaces. (h) The dimer of the chains C1 and C2, shown in the back view as cartoons.

The two distinct dimerization patterns, A-B and C1-C2 were aligned having the RMSD value of 0.716. The salt bridge contributors of both A-B and C1-C2 dimers were presented in Table 3.3 as a list and as visuals in Figure 3.14 and Figure 2.15. The hydrogen bonds between A-B are listed in Table 3.4 and shown in Figure 3.18, the C-C dimer hydrogen bonds are listed in Table 3.5 and visualized in Figure 3.19. The solved structure's (PDB ID: 9V61) dimers' alignment to the mentioned similar structures is presented in Figure 3.20, with RMSD values being 3JQZ: 3.784, 5Z0B: 1.0013 and 8CKS: 2.976

The non-zero RMSD values indicate differences between the two distinct dimerization patterns we suggest, which is also supported by different numbers and contributing residues of the electrostatic interactions within those dimers listed in Table 3.3, Table 3.4, and Table 3.5.

Table 3.3: The PISA-proposed salt bridges between both A-B chains and two C chains listed with bonding atoms and bond distances presented.

	Chain B	Chain A	Distance (Å)		Chain C1	Chain C2	Distance (Å)
1	LYS 212 [NZ]	GLU 208 [OE1]	3.16	**1**	LYS 93 [NZ]	ASP 308 [OD1]	3.49
2	LYS 212 [NZ]	GLU 208 [OE2]	3.99	**2**	LYS 205 [NZ]	GLU 321 [OE2]	3.86
3	GLU 208 [OE1]	LYS 212 [NZ]	2.63	**3**	LYS 212 [NZ]	GLU 208 [OE1]	3.58
4	GLU 208 [OE2]	LYS 212 [NZ]	3.71	**4**	ASP 308 [OD1]	LYS 93 [NZ]	3.49
				5	GLU 321 [OE2]	LYS 205 [NZ]	3.86
				6	GLU 208 [OE1]	LYS 212 [NZ]	3.58

Table 3.4: The PISA-proposed hydrogen bonds between A and B chains listed with bonding atoms and bond distances presented.

	Chain B	*Chain A*	*Distance (Å)*		*Chain B*	*Chain A*	*Distance (Å)*		*Chain B*	*Chain A*	*Distance (Å)*
1	LYS 323 [N]	GLN 204 [O]	3.22	**6**	TYR 148 [OH]	GLU 321 [OE1]	3.14	**11**	ASP 314 [OD2]	GLN 104 [NE2]	3.59
2	LYS 212 [NZ]	GLU 208 [OE1]	3.16	**7**	GLU 266 [O]	LYS 4 [NZ]	3.69	**12**	GLU 321 [OE1]	TYR 148 [OH]	3.61
3	SER 65 [OG]	GLU 227 [OE1]	3.10	**8**	GLU 227 [OE2]	SER 65 [OG]	3.34	**13**	ALA 320 [O]	LYS 205 [NZ]	2.70
4	GLN 104 [NE2]	ASP 314 [OD2]	3.45	**9**	GLU 227 [OE2]	THR 68 [OG1]	3.81	**14**	GLU 208 [OE1]	LYS 212 [NZ]	2.63
5	GLN 104 [NE2]	ASN 318 [OD1]	2.91	**10**	ASN 318 [OD1]	GLN 104 [NE2]	2.98	**15**	GLN 204 [O]	LYS 323 [N]	3.22

Table 3.5: The PISA-proposed hydrogen bonds between the two C chains listed with bonding atoms and bond distances presented.

	Chain C1	***Chain C2***	***Distance (Å)***		***Chain C1***	***Chain C2***	***Distance (Å)***		***Chain C1***	***Chain C2***	***Distance (Å)***
1	LYS 4 [NZ]	GLU 266 [O]	2.68	**7**	TYR 148 [OH]	GLU 321 [OE1]	3.20	**13**	GLU 227 [OE2]	THR 68 [OG1]	3.32
2	SER 65 [OG]	GLU 227 [OE1]	3.48	**8**	LYS 205 [NZ]	GLU 321 [OE2]	3.86	**14**	ASP 314 [OD2]	GLN 104 [NE2]	2.86
3	SER 65 [OG]	GLU 227 [OE2]	3.14	**9**	LYS 323 [N]	GLN 204 [O]	3.24	**15**	ASN 318 [OD1]	GLN 104 [NE2]	2.89
4	THR 68 [OG1]	GLU 227 [OE2]	3.32	**10**	GLU 266 [O]	LYS 4 [NZ]	2.68	**16**	GLU 321 [OE1]	TYR 148 [OH]	3.20
5	GLN 104[NE2]	ASN 318 [OD1]	2.89	**11**	GLU 227 [OE1]	SER 65 [OG]	3.48	**17**	GLU 321 [OE2]	LYS 205 [NZ]	3.86
6	GLN 104 [NE2]	ASP 314 [OD2]	2.86	**12**	GLU 227 [OE2]	SER 65 [OG]	3.14	**18**	GLN 204 [O]	LYS 323 [N]	3.24

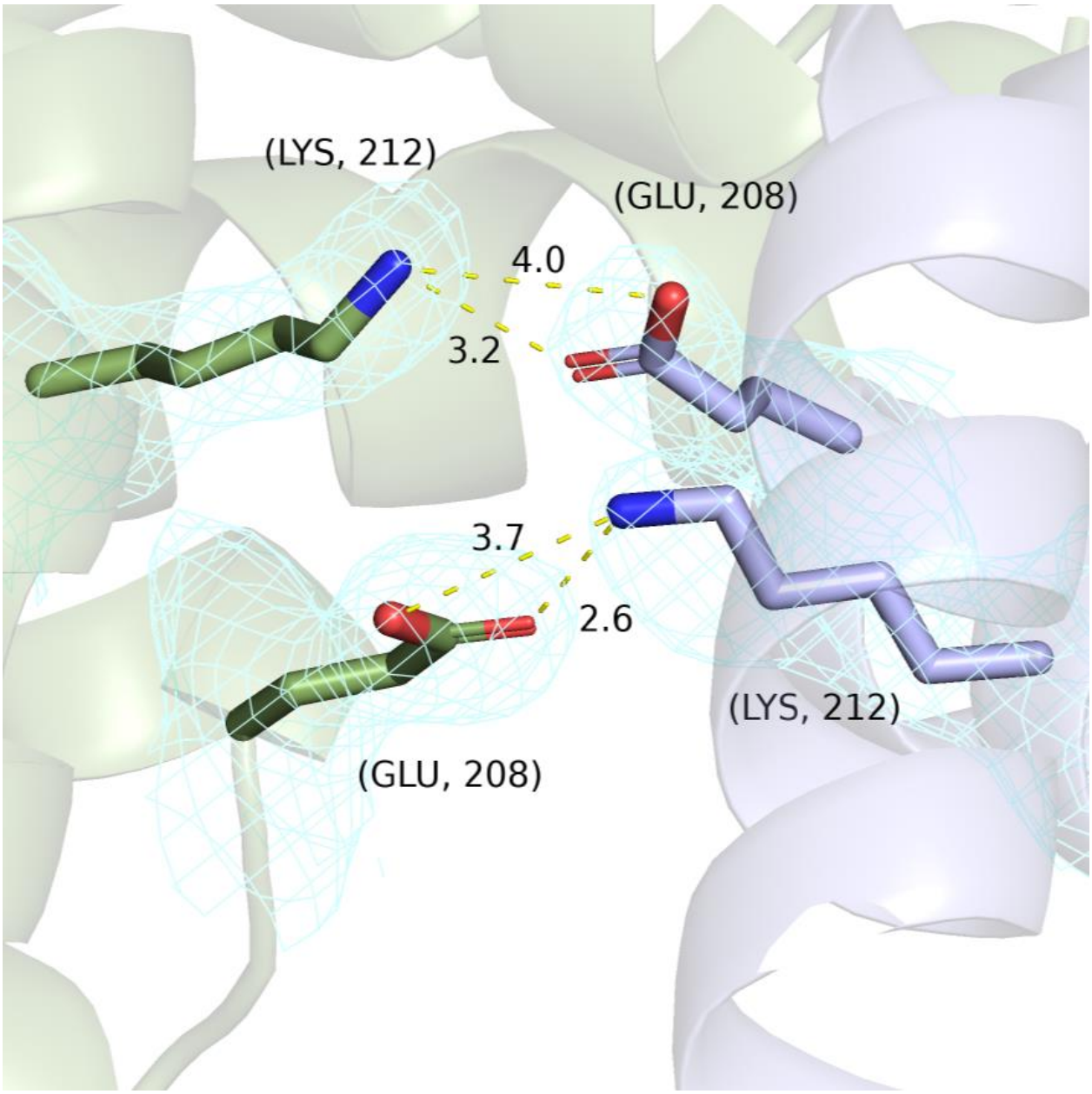

Figure 3.16: The salt bridges presented by PISA between chains A and B are shown with labels and distances. The cyan mesh corresponds to the electron cloud, the green-backboned protein is Chain B, and the blue-colored protein is Chain A.

The Pisa-proposed salt bridges between chains A and B being mirrored indicate that Lys212 and Glu208 are key residues contributing to the proposed dimerization. Both residues being flexible also suggests this interaction can be interfered with.

The salt bridges between the two C chains also include mirrored Lys212 and Glu208. However, the salt bridge network in the chain C dimer is much more extensive and includes other residues making them more versatile and allowing combinations of

interferences to be possible due to more mutagenesis targets.

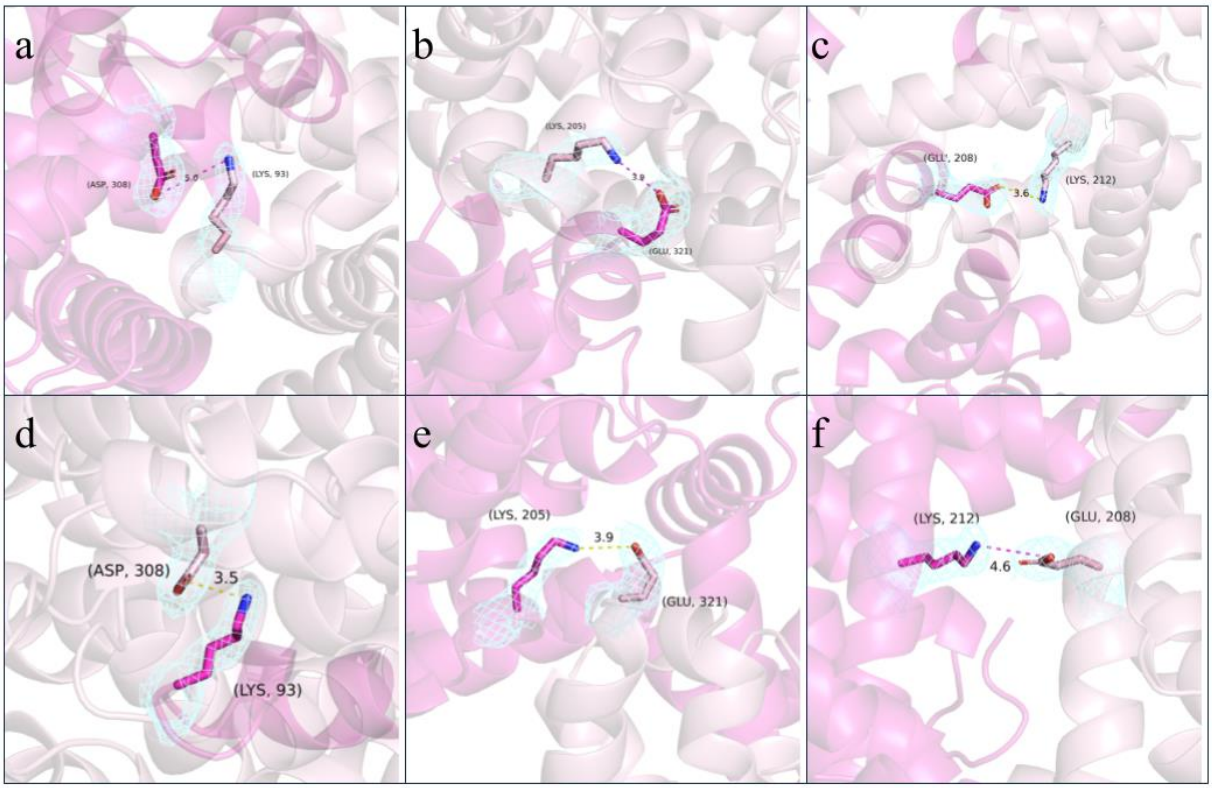

Figure 3.17: The salt bridges presented by PISA between two chain Cs are shown with labels and distances. (a) The salt bridge numbered 1 (Chain C1 Lys93NZ and Chain C2 Asp308OD1) is shown. (b) The salt bridge numbered 2 (Chain C1 Lys205NZ and Chain C2 Glu321OE2) is shown. (c) The salt bridge numbered 3 (Chain C1 Lys212NZ and Chain C2 Glu208OE1) is shown. (d) The salt bridge numbered 4 (Chain C1 Asp308OD1 and Chain C2 Lys93NZ) is shown. (e) The salt bridge numbered 5 (Chain C1 Glu321OE2 and Chain C2 Lys205NZ) is shown. (f) The salt bridge numbered 6 (Chain C1 Glu208OE1 and Lys212NZ) is shown.

The A-B dimer has 15 hydrogen bonds contributing to the dimerization as given in Table 3.4, and the C-C dimer has 18 hydrogen bonds. The interaction and the electrostatic pull being dispersed to this many points makes fine-tuning the interaction strength plausible.

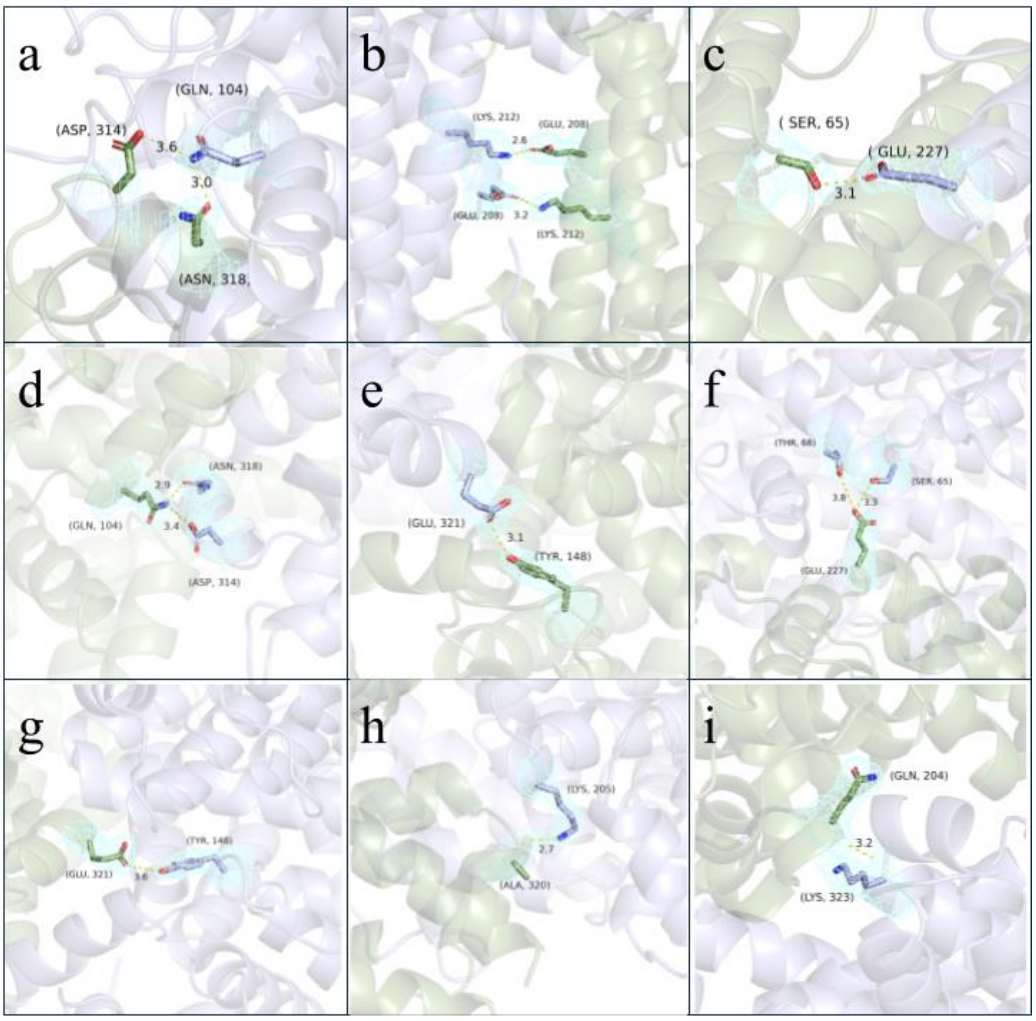

Figure 3.18: The hydrogen bonds presented by PISA between chains A and B are shown with labels and distances. The blue mesh is the observed electron cloud, prepared in pymol software. (a) The hydrogen bonds numbered 10 (Chain B Asn318OD1 and Chain A Gln104NE2) and 11 (Chain B Asp314OD2 and Chain A Gln104NE2) are shown. (b) The hydrogen bonds numbered 2 (Chain B Lys212NZ and Chain A Glu208OE1) and 14 (Chain B Glu208OE1 and Chain A Lys212NZ) are shown. (c) The hydrogen bond numbered 3 (Chain B Ser65OG and Chain A Glu227OE1) is shown. (d) The hydrogen bonds numbered 4 (Chain B Gln104NE2 and Chain A Asp314OD2) and 5 (Chain B Gln104NE2 and Chain A Asn318OD1) are shown. (e) The hydrogen bond numbered 6 (Chain B Tyr148OH and Chain A Glu321OE1) is shown. (f) The hydrogen bonds numbered 8 (Chain B Glu227OE2 and Chain A Ser65OG) and 9 (Chain B Glu227OE2 and Chain A Thr68OG1) are shown. (g) The hydrogen bond numbered 12 (Chain B Glu321OE1 and Chain A Gln104NE2) is shown. (h) The hydrogen bond numbered 13 (Chain B Ala320O and Chain A Lys205NZ) is shown. (i) The hydrogen bond numbered 15 (Chain B Gln204O and Chain A Lys323N) is shown.

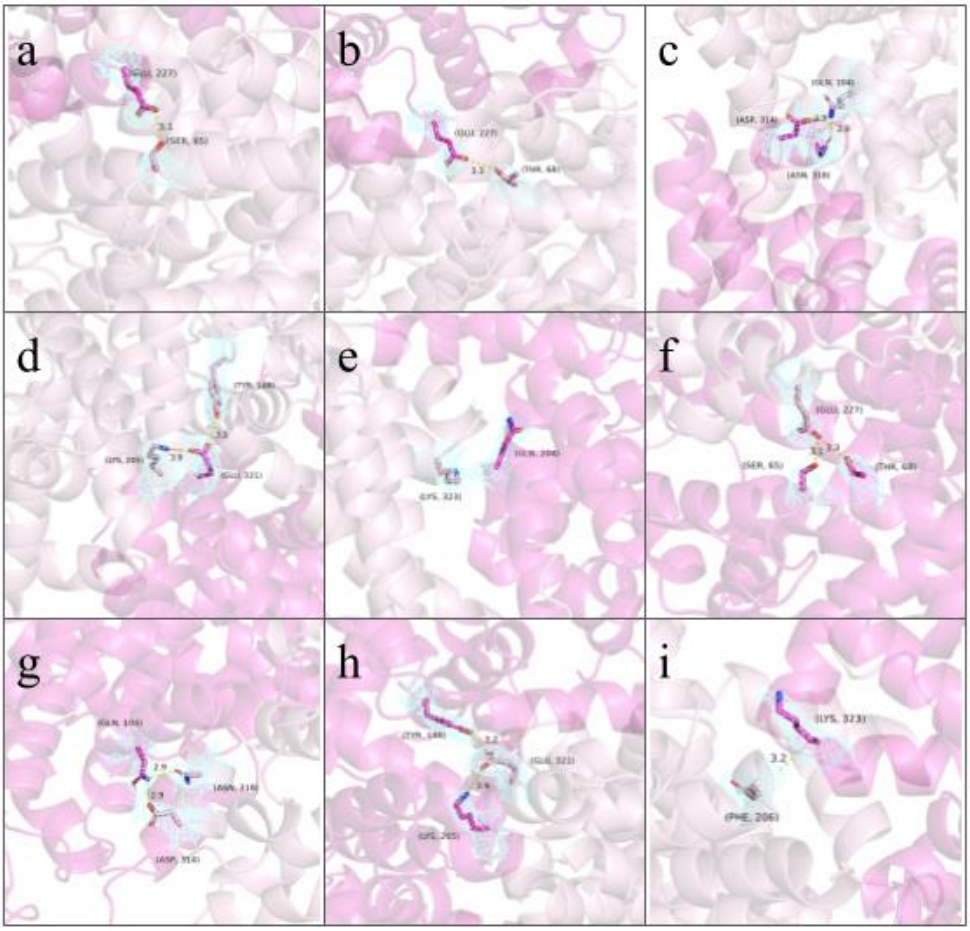

Figure 3.19: The hydrogen bonds presented by PISA between two chain Cs are shown with labels and distances. The blue mesh is the observed electron cloud, prepared in Pymol software. (a) The hydrogen bonds numbered 2 (Chain C1 Ser65OG and Chain C2 Glu227OE1) and 3 (Chain C1 Ser65OG and Chain C2 Glu227OE2) are shown. (b) The hydrogen bond numbered 4 (Chain C1 Thr68OG1 and Chain C2 Glu227OE2) is shown. (c) The hydrogen bonds numbered 5 (Chain C1 Gln104NE2 and Chain C2 Asn318OD1) and 6 (Chain C1 Gln104NE2 and Chain C2 Asp314OD2) are shown. (d) The hydrogen bonds numbered 7 (Chain C1 Tyr148OH and Chain C2 Glu321OE1) and 8 (Chain C1 Lys205NZ and Chain C1 Gln204O) are shown. (e) The hydrogen bond numbered 9 (Chain C1 Lys323N and Chain C2 Gln204O) is shown. (f) The hydrogen bonds numbered 11 (Chain C1 Glu227OE1 and Chain C2 Ser65OG), 12 (Chain C1 Glu227OE2 and Chain C2 Ser65OG) and 13 (Chain C1 Glu227OE2 and Chain C2 Thr68OG1) are shown. (g) The hydrogen bonds numbered 14 (Chain C1 Asp314OD2 and Chain C2 Gln104NE2) and 15 (Chain C1 Asn218OD1 and Chain C2 Gln104NE2) are shown. (h) The hydrogen bonds numbered 16 (Chain C1 Glu321OE1 and Chain C2 Tyr148OH) and 17 (Chain C1 Glu321OE2 and Chain C2 Lys205NZ) are shown. (i) The hydrogen bond numbered 18 (Chain C1 Gln204O and Chain C2 Lys323N) is shown.

The listed and discussed electrostatic interactions are supported by the presented electron clouds as presented in Figure 3.18 and Figure 3.19, the electrons being indirectly observed at those 3D coordinates indicate these residues' listed interactions are not an artifact from the processing steps but an actual observed phenomenon.

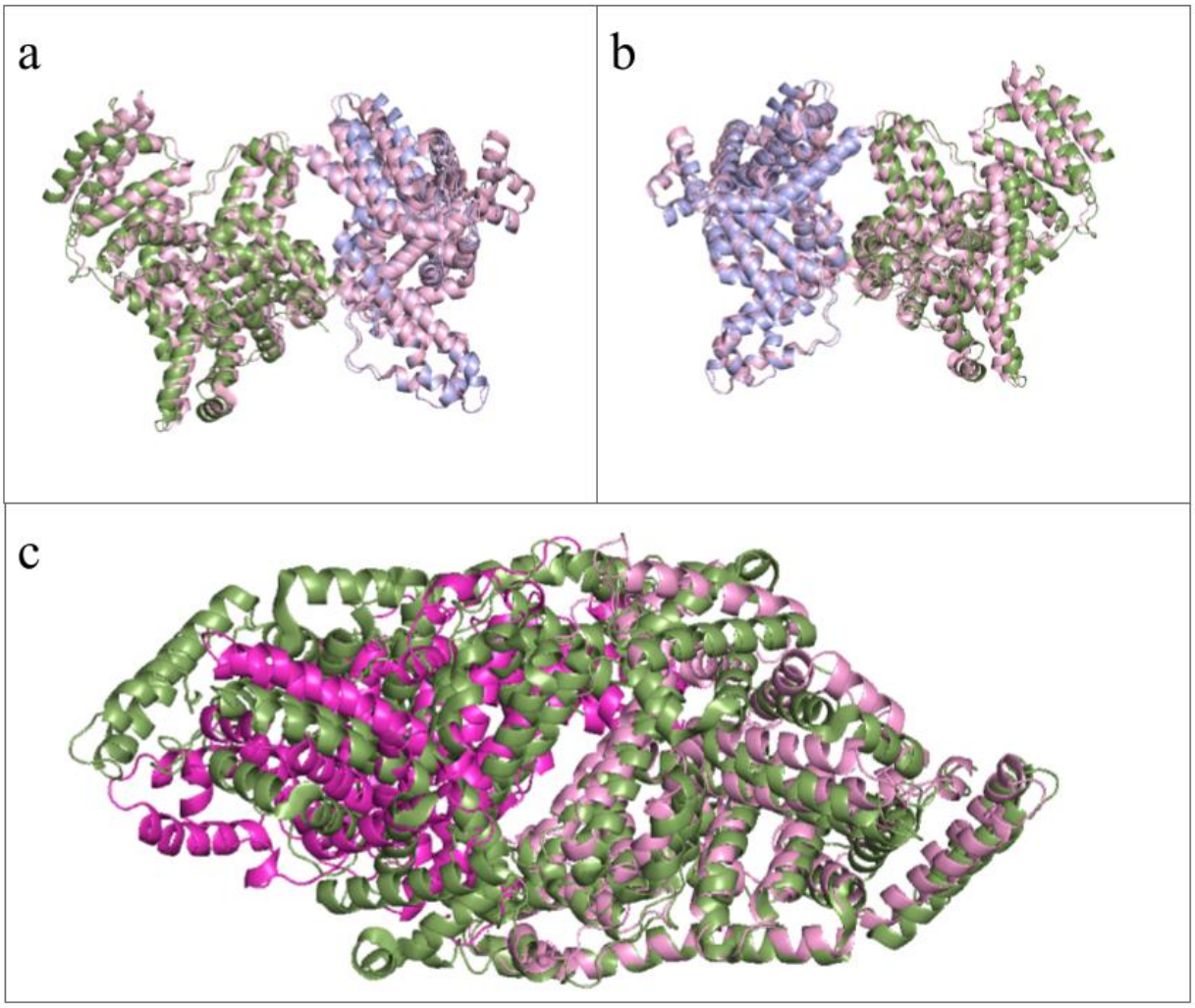

Figure 3.20: Our structure aligned to the other similar interface area structures 5Z0B (RMSD 1.0013) and 8CKS (RMSD 2.976). (a) the solved structure's A (blue) and B (green) chains aligned to 5Z0B (pink) dimer, front view. (b) the solved structure's A (blue) and B (green) chains aligned to 5Z0B dimer, back view. (c) the solved structure's C1 (pink) and C2 (magenta) chains aligned to 8CKS (green) dimer, front view.

The RMSD values between other comparatively high interface areas having structures show not too much differences indicating those are very close patterns with slight shifts in positions. The pattern we discuss being observed in other structures as well also supports the significance and relevance of the pattern in protein dimerization dynamics.

3.5 Deposited Structure statistics and comparisons

Other than a trimer (Park et al., 2021) and another dimer (PDB accession codes: 5Z0B and 8CKS) there is no other crystal structure among the hundreds of structures in PDB with an interaction surface larger than 1300 Å different from our two dimers. In addition to the interaction surface area, these structures also have out-of-ordinary space groups in their crystals, Our solved structures and 8CKS are *I 1 2 1* and the only reversible dimer 3JQZ is the only *I 41*. How rare this high interface area and these specific space groups are, are presented in Figure 3.21 and Figure 3.22 respectively.

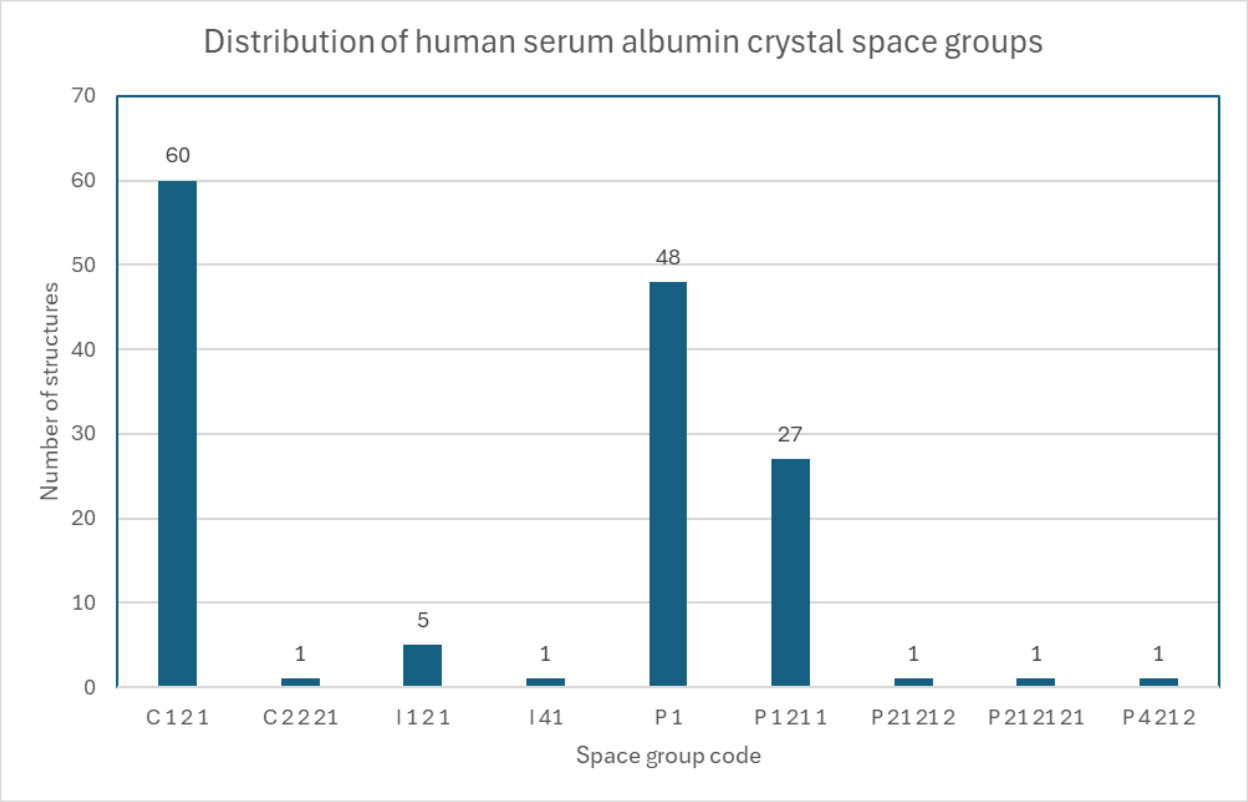

Figure 3.21: The histogram depicting the distribution of the space groups' of human serum albumin crystals in all crystal structures in PDB, heterogeneous (having more than one unique peptide chain) and non-crystal (cryo-EM and such) are excluded. The two proposed dimers in this paper (A-B and C-C) are included and counted in the I 1 2 1 space group.

The histogram of the interface areas given in Figure 3.22 has an empty space between 1300Å and 1500Å giving the visual of two separate normal distributions. The visualization of the interface area in all HSA crystals appears as two distinct bell curves suggesting these can be inherent differences between two clusters.

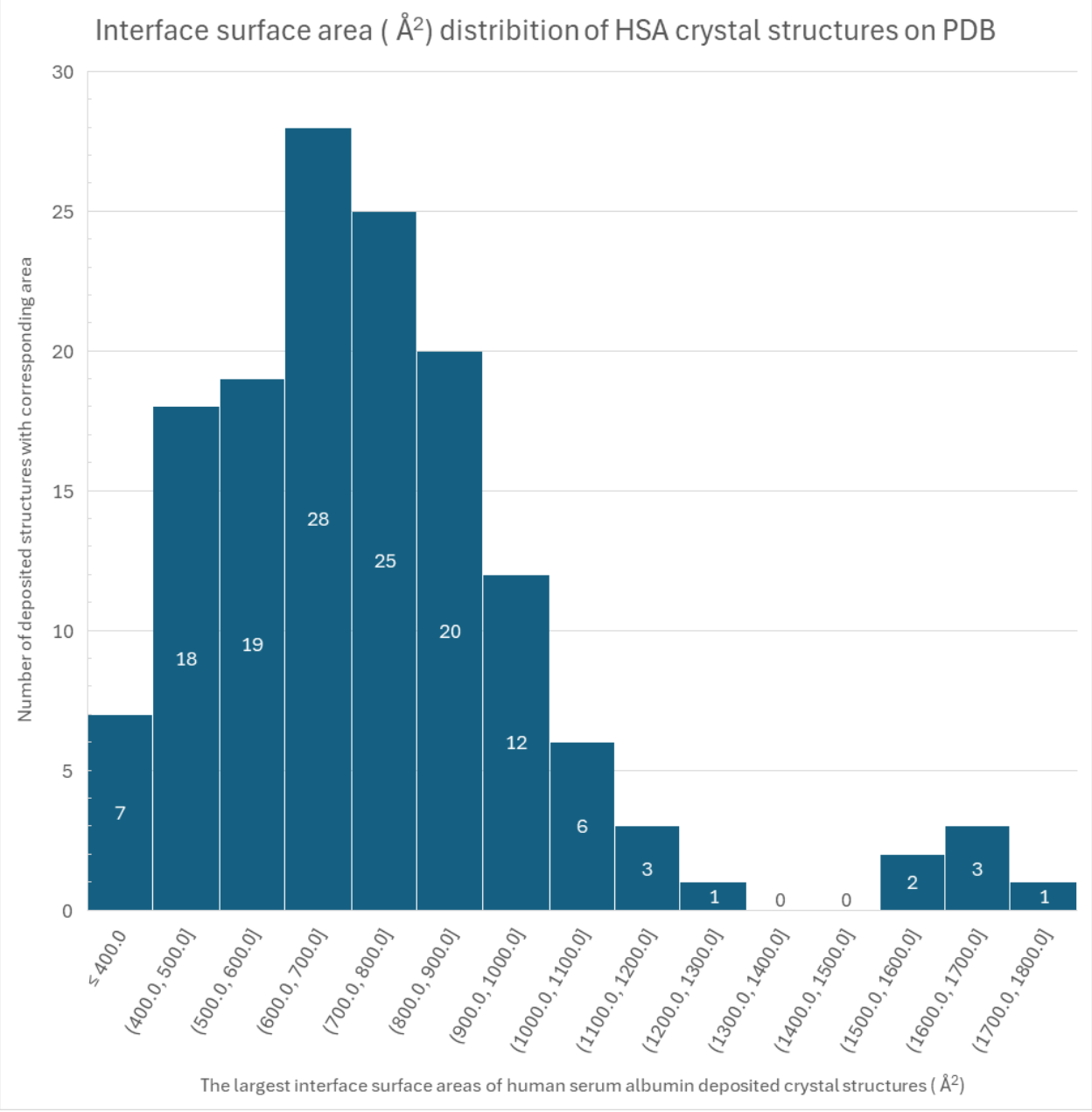

Figure 3.22: The histogram depicting the distribution of the interface surface areas between human serum albumin chains in all HSA crystal structures in PDB, heterogeneous (having more than one unique peptide chain) and non-crystal (cryo-EM and such) are excluded. The two proposed dimers in this paper (A-B and C-C) are included and counted in the 1600.0-1700.0 Å² range.

3.6 Dipyridamole Dockings

The native ligand warfarin was docked into the active site. After the docking procedure, the positions of identical atoms between the native ligand and the docked ligand were compared, and RMSD was calculated. RMSD calculation is a crucial method for validating the docking procedure, and an RMSD value under 2Å indicates that the docking procedure was close enough to the experimental result. Using DockRMSD script designed by Zhangg Group (Abdulilah Ece, 2023), the RMSD value of our docked ligand was calculated. The RMSD value was calculated to be 0.878Å. Concluding that the docking procedure was close enough to the experimental result, we docked dipyridamole into the same active site of HSA.

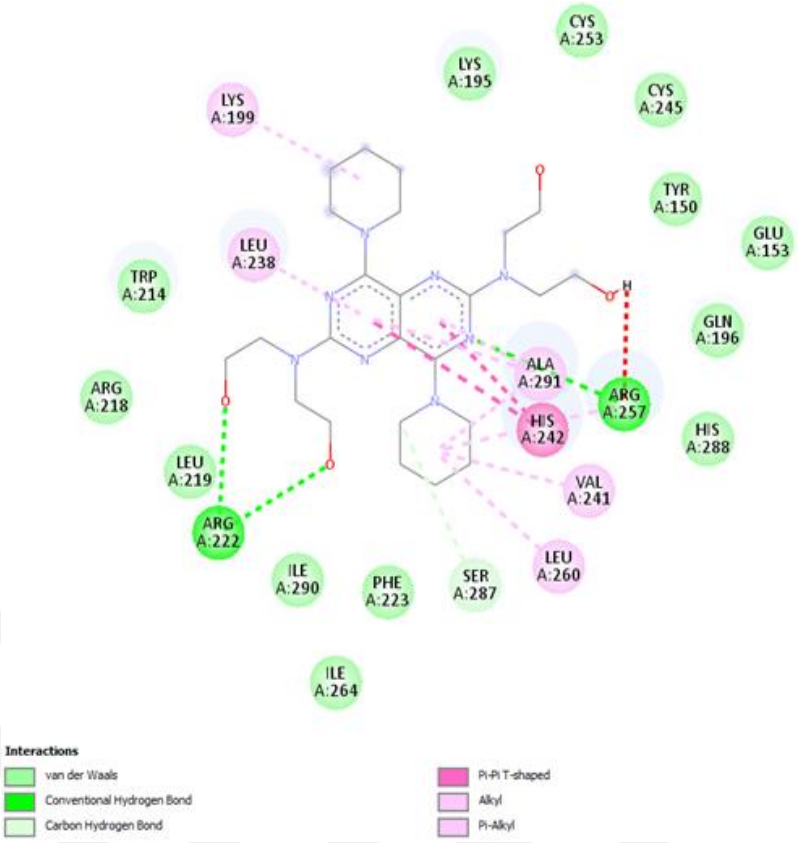

Figure 3.23: The 2D interaction map and diagram between dipyridamole and the amino acid residues of the HSA active site are depicted.

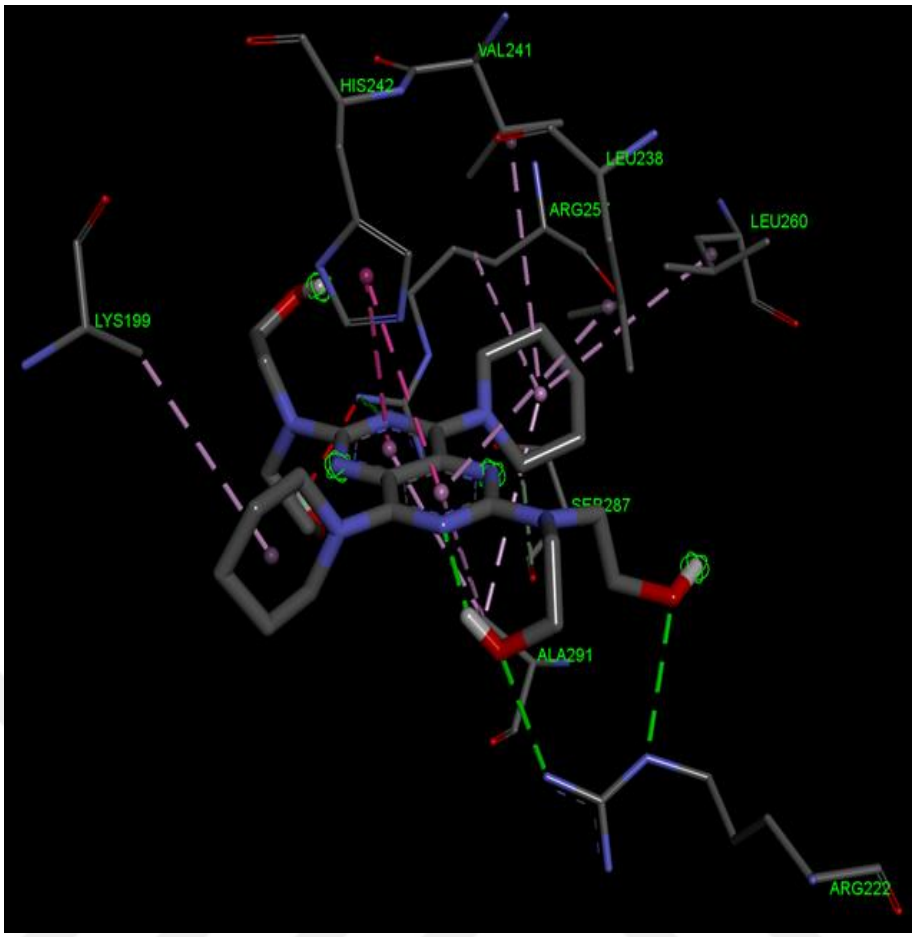

Figure 3.24: The 3D interaction map and diagram between dipyridamole and the amino acid residues of the HSA active site are depicted.

Chapter 4

DISCUSSION AND CONCLUSION

Molecular docking results show that dipyridamole shows significant affinity towards the active site of the HSA protein by forming several intermolecular interactions in the residues of the active site. The docked pose with the highest scoring cluster is demonstrated in Figure 1, showing both the 2D and 3D interactions of dipyridamole and the active site of HSA. As shown in Figure 5 and Figure 6, it is apparent that the dipyridamole forms a strong hydrogen bond between the ARG222 residue with one of its hydroxyl tails attached to both ends of the amines in the structure. There is also a hydrogen bond between the aromatic heterocycle of the ligand and the ARG257 residue. Furthermore, aromatic rings in dipyridamole interact with the HIS242 residue by forming π-π interactions with the aromatic ring in the histidine residue. Additionally, there are several alkyl and π-alkyl interactions between LYS199, LEU238, VAL241, LEU260, and ALA291 residues and aromatic rings and the saturated heterocycles of dipyridamole. Furthermore, it can also be deduced that this binding event may affect the distribution of dipyridamole in the bloodstream, resulting in a direct effect on the pharmacokinetic profile of dipyridamole (Fanali et al., 2012).

HSA dimerization patterns can offer novel insights into nanoparticle generation and recombinant-HSA-dependent delivery systems hence this research demonstrates two particular patterns of dimerization. Protein dimerization can be facilitated by electrostatic interactions hence the salt bridges and hydrogen bonds in the proposed HSA dimerization are characterized and identified as seen in Table 3.3, Table 3.5, and Table 3.5 (Grassmann et al., 2023).

The interface area histogram in Figure 3.24 shows that the distribution of the area in HSA crystals is arranged in two distinct normal distribution peaks. The first one consists of monomer crystallization and the second smaller one suggests dimerization occurring before crystallization nucleation, the two peaks having a large gap between them suggest the events leading to crystallization are different. The concentration of the unusual space groups such as *I 41* and *I 1 2 1* is also a notable difference further suggesting the crystallized units are different. The single highest surface area above 1700Å belongs to a priorly established HSA non-covalent dimer structure supporting the significance of our dimerization patterns' plausibility and exploitability regarding in vivo interactions of Nanoparticle generations.

The overwhelming interface area and comparatively large number of electrostatic interactions suggest an inherent interaction in the dimers that is different than crystallization artifacts suggesting somewhere in the process HSA monomer-dimer equilibrium shifted to favor dimers more. The chromatograms given in Figure 3.1, Figure 3.2, and Figure 3.3 suggest this happens after purification possibly during the extensive waiting period of gradual concentration increase in the sitting drop vapor diffusion crystallography. Once compared with the other structures with unusually high interface area in Figure 3.22, it is observed that there are differences between the structures even though interacting surfaces are the same with slight interacting residue differences between them. In Figures 13-16 the electrostatic interactions were given with the electron clouds visible to ensure this protein folding is confident in the interacting residues and is observed and not just calculated during the molecular replacement.

In HSA-based drug delivery, it is important to tailor the approach based on the drug and the drug's binding site on the protein, our dimerization patterns do not alter Sudlow's drug binding sites I and II hence would not negatively affect the bindings of most drug active ingredients. It may also be possible to alter the strength, association, and dissociation patterns of HSA nanoparticles and recombinant-dimer-HSAs via altering the identified residue using mutagenesis or targeted post-translational modifications. The increasing knowledge of possible HSA dimerization patterns may introduce new parameters, the protein itself and a few key residues, to the discipline of HSA nanoparticle research hence we recommend nanoparticle efficiency comparison experiments with HSA mutants may lead to important practical discoveries in the field.

The identification and characterization of two novel HSA dimerization interfaces provide compelling evidence for previously unlooked plasticity in albumin self-interaction. The extensive electrostatic and hydrogen bonding interactions, coupled with their large interface surface areas, suggest that these dimers may hold biological or application-relevant significance rather than mere crystallographic artifacts. As these interactions do not compromise known pharmacologically relevant binding domains, they present promising frameworks for engineering stable HSA-based nanoparticles. Moreover, these findings propose a new variable in the field of albumin nanoparticle engineering, namely, the modulation of protein-protein interfaces. Future investigations into mutagenesis or post-translational modifications targeting the residues involved in these dimer interfaces may yield tunable nanoparticle constructs with altered stability and targeting efficiency. These insights not only contribute to the structural biology of HSA but also reinforce the usage of HSA dimers in advanced drug delivery platforms. As it comes to the dipyridamole interaction with Sudlow's site I, there is evidence that this dimerization pattern-based

nanoparticles or other biotechnological carrier agents would not change the binding dynamics.

Bibliography

Abdulilah Ece. (2023). Computer-aided drug design. *BMC Chemistry*, *17*(1). https://doi.org/10.1186/s13065-023-00939-w

Afrin, S., Rahman, Y., Sarwar, T., Ansari, M. O., Ahmed, S., Rizvi, M. A., Shadab, G. G. Hammad. A., & Tabish, M. (2022). Cytotoxic and genotoxic evaluation of dipyridamole and its alternative therapeutic potential in cancer therapy: an in vitro and in vivo approach. *Journal of Molecular Structure*, *1249*, 131626. https://doi.org/10.1016/j.molstruc.2021.131626

Al-Tubuly, A. A. (2000). SDS-PAGE and Western Blotting. *Diagnostic and Therapeutic Antibodies*, *40*, 391–405. https://doi.org/10.1385/1-59259-076-4:391

Alinovskaya, L. I., Sedykh, S. E., Ivanisenko, N. V., Soboleva, S. E., & Nevinsky, G. A. (2018). How human serum albumin recognizes DNA and RNA. *Biological Chemistry*, *399*(4), 347–360. https://doi.org/10.1515/hsz-2017-0243

Archuleta, A. (2024). *SDS-PAGE: The science behind all those bubbles | PhosphoSolutions*. Antibodies Incorporated. https://www.antibodiesinc.com/pages/sds-page-demystified

Arnold, S. A., & Brekken, R. A. (2009). SPARC: a matricellular regulator of tumorigenesis. *Journal of Cell Communication and Signaling*, *3*(3-4), 255–273. https://doi.org/10.1007/s12079-009-0072-4

Ashraf, S., Qaiser, H., Tariq, S., Khalid, A., Makeen, H. A., Alhazmi, H. A., & Zaheer Ul-Haq. (2023). Unraveling the versatility of human serum albumin – A comprehensive review of its biological significance and therapeutic potential. *Current Research in Structural Biology*, *6*, 100114–100114. https://doi.org/10.1016/j.crstbi.2023.100114

BIOVIA. (2023, September 8). *Discovery Studio*. Dassault Systèmes. https://www.3ds.com/products/biovia/discovery-studio

Bjørk, A., Dimitrios Mantzilas, Reidun Sirevåg, & Eijsink, V. G. H. (2003). Electrostatic interactions across the dimer–dimer interface contribute to the pH-dependent stability of a tetrameric malate dehydrogenase. *FEBS Letters*, *553*(3), 423–426. https://doi.org/10.1016/s0014-5793(03)01076-7

Bunaciu, A. A., Udriştioiu, E. gabriela, & Aboul-Enein, H. Y. (2015). X-Ray Diffraction: Instrumentation and Applications. *Critical Reviews in Analytical Chemistry*, *45*(4), 289–299. https://doi.org/10.1080/10408347.2014.949616

Chinnaswamy Tiruppathi, Song, W., Magnus Bergenfeldt, Sass, P., & Malik, A. B. (1997). Gp60 Activation Mediates Albumin Transcytosis in Endothelial Cells by Tyrosine Kinase-dependent Pathway. *Journal of Biological Chemistry*, *272*(41), 25968–25975. https://doi.org/10.1074/jbc.272.41.25968

Chubarov, A., Spitsyna, A., Krumkacheva, O., Mitin, D., Suvorov, D., Tormyshev, V., Fedin, M., Bowman, M. K., & Bagryanskaya, E. (2020). Reversible Dimerization of Human Serum Albumin. *Molecules (Basel, Switzerland)*, *26*(1), E108. https://doi.org/10.3390/molecules26010108

Dixon, B. S., Beck, G. J., Vazquez, M. A., Greenberg, A., Delmez, J. A., Allon, M., Dember, L. M., Himmelfarb, J., Gassman, J. J., Greene, T., Radeva, M., Davidson, I., T. Alp Ikizler, Braden, G., Fenves, A. Z., Kaufman, J. C., Cotton, J., Martin, K. J., McNeil, J. A., & Rahman, A. (2009). Effect of Dipyridamole plus Aspirin on Hemodialysis Graft Patency. *The New England Journal of Medicine*, *360*(21), 2191–2201. https://doi.org/10.1056/nejmoa0805840

Dumetz, A. C., Chockla, A. M., Kaler, E. W., & Lenhoff, A. M. (2008). Protein Phase Behavior in Aqueous Solutions: Crystallization, Liquid-Liquid Phase Separation, Gels,

and Aggregates. *Biophysical Journal*, *94*(2), 570–583. https://doi.org/10.1529/biophysj.107.116152

Fanali, G., di Masi, A., Trezza, V., Marino, M., Fasano, M., & Ascenzi, P. (2012). Human serum albumin: From bench to bedside. *Molecular Aspects of Medicine*, *33*(3), 209–290. https://doi.org/10.1016/j.mam.2011.12.002

Fata-Hartley, C. L., & Palmenberg, A. C. (2005). Dipyridamole Reversibly Inhibits Mengovirus RNA Replication. *Journal of Virology*, *79*(17), 11062–11070. https://doi.org/10.1128/jvi.79.17.11062-11070.2005

Ghuman, J., Zunszain, P. A., Petitpas, I., Bhattacharya, A. A., Otagiri, M., & Curry, S. (2005). Structural Basis of the Drug-binding Specificity of Human Serum Albumin. *Journal of Molecular Biology*, *353*(1), 38–52. https://doi.org/10.1016/j.jmb.2005.07.075

Grassmann, G., Di Rienzo, L., Gosti, G., Leonetti, M., Ruocco, G., Miotto, M., & Milanetti, E. (2023). Electrostatic complementarity at the interface drives transient protein-protein interactions. *Scientific Reports*, *13*(1). https://doi.org/10.1038/s41598-023-37130-z

Gurung, A. B., Ali, M. A., Lee, J., Farah, M. A., Khalid Mashay Al-Anazi, & Sami, H. (2021). Molecular modelling studies unveil potential binding sites on human serum albumin for selected experimental and in silico COVID-19 drug candidate molecules. *Saudi Journal of Biological Sciences*, *29*(1), 53–64. https://doi.org/10.1016/j.sjbs.2021.09.042

Hanwell, M. D., Curtis, D. E., Lonie, D. C., Vandermeersch, T., Zurek, E., & Hutchison, G. R. (2012). Avogadro: an advanced semantic chemical editor, visualization, and analysis platform. *Journal of Cheminformatics*, *4*(1). https://doi.org/10.1186/1758-2946-4-17

Harker, L. A., & Kadatz, R. A. (1983). Mechanism of action of dipyridamole. *Thrombosis Research. Supplement*, *4*, 39–46. https://doi.org/10.1016/0049-3848(83)90356-0

Harris, G., Bradshaw, M. L., Halsall, D. J., Scott, D. J., Unwin, R. J., & Norden, A. G. W. (2024). Is there reversible dimerization of albumin in blood plasma? And does it matter? *Experimental Physiology*, *109*(10), 1663–1671. https://doi.org/10.1113/ep092012

Hornok, V. (2021). Serum Albumin Nanoparticles: Problems and Prospects. *Polymers*, *13*(21), 3759. https://doi.org/10.3390/polym13213759

Ji, Q., Zhu, H., Qin, Y., Zhang, R., Wang, L., Zhang, E., Zhou, X., & Meng, R. (2024). GP60 and SPARC as albumin receptors: key targeted sites for the delivery of antitumor drugs. *Frontiers in Pharmacology*, *15*. https://doi.org/10.3389/fphar.2024.1329636

Kalakonda, A., John, S., & Jenkins, B. A. (2022). *Physiology, Bilirubin*. National Library of Medicine; StatPearls Publishing. https://www.ncbi.nlm.nih.gov/books/NBK470290/

Kerndt, C. C., & Shivaraj Nagalli. (2023, July 3). *Dipyridamole*. Nih.gov; StatPearls Publishing. http://www.ncbi.nlm.nih.gov/books/NBK554455/

Kim Langmach Hein, Ulrich Kragh-Hansen, J. Preben Morth, Jeppesen, M. D., Otzen, D., Møller, J. V., & Nissen, P. (2010). Crystallographic analysis reveals a unique lidocaine binding site on human serum albumin. *Journal of Structural Biology*, *171*(3), 353–360. https://doi.org/10.1016/j.jsb.2010.03.014

Kratz, F., & Elsadek, B. (2012). Clinical impact of serum proteins on drug delivery. *Journal of Controlled Release*, *161*(2), 429–445. https://doi.org/10.1016/j.jconrel.2011.11.028

Krissinel, E., & Henrick, K. (2007). Inference of Macromolecular Assemblies from Crystalline State. *Journal of Molecular Biology*, *372*(3), 774–797. https://doi.org/10.1016/j.jmb.2007.05.022

Kumari, V. B. C., Patil, S. M., Ramu, R., Shirahatti, P. S., Kumar, N., Sowmya, B. P., Egbuna, C., Uche, C. Z., & Patrick-Iwuanyanwu, K. C. (2022). Chromatographic techniques: types, principles, and applications. *Analytical Techniques in Biosciences*, 73–101. https://doi.org/10.1016/b978-0-12-822654-4.00013-0

McPherson, A., & Gavira, J. A. (2013). Introduction to protein crystallization. *Acta Crystallographica Section F Structural Biology Communications*, *70*(1), 2–20. https://doi.org/10.1107/s2053230x13033141

Mehmet Gül, Ayan, E., Ebru Destan, J Austin Johnson, Alaleh Shafiei, Abdullah Kepceoğlu, Yilmaz, M., Fatma Betül Ertem, İlkin Yapici, Bilge Tosun, Nilüfer Baldir, Tokay, N., Zeliş Nergiz, Gözde Karakadioğlu, Seyide Seda Paydos, Cahine Kulakman, Cengiz Kaan Ferah, Ömür Güven, Necati Atalay, & Enver Kamil Akcan. (2023). Rapid and efficient ambient temperature X-ray crystal structure determination at Turkish Light Source. *Scientific Reports*, *13*(1). https://doi.org/10.1038/s41598-023-33989-0

Merlot, A. M., Kalinowski, D. S., & Richardson, D. R. (2014). Unraveling the mysteries of serum albumin - more than just a serum protein. *Frontiers in Physiology*, *5*. https://doi.org/10.3389/fphys.2014.00299

Mishra, V., & Heath, R. J. (2021). Structural and Biochemical Features of Human Serum Albumin Essential for Eukaryotic Cell Culture. *International Journal of Molecular Sciences*, *22*(16), 8411. https://doi.org/10.3390/ijms22168411

Ó'Fágáin, C., Cummins, P. M., & O'Connor, B. F. (2010). Gel-Filtration Chromatography. In *Methods in Molecular Biology* (pp. 25–33). https://doi.org/10.1007/978-1-60761-913-0_2

Park, J., Kim, M.-S., Park, T., Kim, Y. H., & Shin, D. H. (2021). Crystal structure of pharmaceutical-grade human serum albumin. *International Journal of Biological Macromolecules*, *166*, 221–228. https://doi.org/10.1016/j.ijbiomac.2020.10.152

Patel, S., Aundhia, C., Seth, A., Shah, N., Gohil, D., & Pandya, K. (2021). Human Serum Albumin: A Novel Drug Delivery Carrier System. *Journal of Pharmaceutical Research International*, 18–24. https://doi.org/10.9734/jpri/2021/v33i44b32648

Petitpas, I., Bhattacharya, A. A., Twine, S., East, M., & Curry, S. (2001). Crystal structure analysis of warfarin binding to human serum albumin: anatomy of drug site I. *The Journal of Biological Chemistry*, *276*(25), 22804–22809. https://doi.org/10.1074/jbc.M100575200

Porath, J., & Flodin, P. (1987). Gel filtration: A method for desalting and group separation. *Chromatographia*, *23*(5), 365–369. https://doi.org/10.1007/bf02316184

Qu, N., Song, K., Ji, Y., Liu, M., Chen, L., Lee, R., & Teng, L. (2024). Albumin Nanoparticle-Based Drug Delivery Systems. *International Journal of Nanomedicine*, *Volume 19*, 6945–6980. https://doi.org/10.2147/ijn.s467876

Smyth, M. S., & Martin, J. H. J. (2000). X Ray Crystallography. *Molecular Pathology*, *53*(1), 8–14. https://doi.org/10.1136/mp.53.1.8

Srivastava, N., Singh, A., Kumari, P., Nishad, J. H., Gautam, V. S., Yadav, M., Bharti, R., Kumar, D., & Kharwar, R. N. (2021). Advances in extraction technologies: isolation and purification of bioactive compounds from biological materials. *Natural Bioactive Compounds*, 409–433. https://doi.org/10.1016/b978-0-12-820655-3.00021-5

Sudlow, G., Birkett, D. J., & Wade, D. N. (1975). The characterization of two specific drug binding sites on human serum albumin. *PubMed*, *11*(6), 824–832.

Taguchi, K., Giam Chuang, V. T., Maruyama, T., & Otagiri, M. (2012). Pharmaceutical Aspects of the Recombinant Human Serum Albumin Dimer: Structural Characteristics, Biological Properties, and Medical Applications. *Journal of Pharmaceutical Sciences*, *101*(9), 3033–3046. https://doi.org/10.1002/jps.23181

Tao, H., Wang, R., Sheng, W., & Zhen, Y. (2021). The development of human serum albumin-based drugs and relevant fusion proteins for cancer therapy. *International Journal of Biological Macromolecules*, *187*, 24–34. https://doi.org/10.1016/j.ijbiomac.2021.07.080

Thermo Fisher Scientific Inc. (2025). *Desalting and Gel Filtration Chromatography | Thermo Fisher Scientific - US*. Thermofisher.com. https://www.thermofisher.com/tr/en/home/life-science/protein-biology/protein-biology-learning-center/protein-biology-resource-library/pierce-protein-methods/desalting-gel-filtration-chromatography.html

Wang, J., Gou, Y., Zhang, Z., Yu, P., Qi, J., Qin, Q., Sun, H., Wu, X., Liang, H., & Yang, F. (2018). Developing an Anticancer Copper(II) Multitarget Pro-Drug Based on the His146 Residue in the IB Subdomain of Modified Human Serum Albumin. *Molecular Pharmaceutics*, *15*(6), 2180–2193. https://doi.org/10.1021/acs.molpharmaceut.8b00045

Wasko, J., Wolszczak, M., Zajaczkowska, Z., Dudek, M., & Kolesinska, B. (2024). Human serum albumin as a potential drug delivery system for N-methylated hot spot insulin analogs inhibiting hormone aggregation. *Bioorganic Chemistry*, *143*, 107104. https://doi.org/10.1016/j.bioorg.2024.107104

Wei, G., Zhang, S., Yu, S., & Lu, W. (2023). Intravital Microscopy Reveals Endothelial Transcytosis Contributing to Significant Tumor Accumulation of Albumin Nanoparticles. *Pharmaceutics*, *15*(2), 519. https://doi.org/10.3390/pharmaceutics15020519

Wlodawer, A., Zbigniew Dauter, & Jaskolski, M. (2017). Protein Crystallography. In *Methods in molecular biology*. Springer Science+Business Media. https://doi.org/10.1007/978-1-4939-7000-1

Xu, S., Luo, W., Zhu, M., Zhao, L., Gao, L., Liang, H., Zhang, Z., & Yang, F. (2025). Correction to “Human Serum Albumin-Platinum(II) Agent Nanoparticles Inhibit Tumor

Growth Through Multimodal Action Against the Tumor Microenvironment." *Molecular Pharmaceutics*. https://doi.org/10.1021/acs.molpharmaceut.5c00050

Yueh, C., Hall, D. R., Xia, B., Padhorny, D., Kozakov, D., & Vajda, S. (2017). ClusPro-DC: Dimer Classification by the Cluspro Server for Protein–Protein Docking. *Journal of Molecular Biology*, *429*(3), 372–381. https://doi.org/10.1016/j.jmb.2016.10.019

Zhivkova, Z. (2015). Studies on Drug – Human Serum Albumin Binding: The Current State of the Matter. *Current Pharmaceutical Design*, *21*(14), 1817–1830. https://doi.org/10.2174/1381612821666150302113710

Appendix A
Chemicals

NaOH	ISOLAB
ALBUMAN	Centurion
HCl	ISOLAB
NaCl	ISOLAB
SDS	Sigma-Aldrich
Tris Base	Sigma-Aldrich
BME	Sigma-Aldrich
Paraffin Oil	Tekkim Kimya

Appendix B
Equipment

AKTA go	Cytiva
Amicon Ultra Centrifugal filters	Merck Millipore
Beckman Allegra 15R Centrifuge	Beckman Coulter
Beckman Avanti J-26S	Beckman Coulter
Beckman Ti-45 Rotor	Beckman Coulter
Branson W250 Sonifier	Branson
Cryotubes	Wuxi NEST Biotechnology
Eppendorf Tubes	Eppendorf New Brunswick
Falcon Tubes	FIRATMED
Innova 44R Incubator Shaker	Eppendorf New Brunswick
Innova 4430R Incubator Shaker	Eppendorf New Brunswick
Kimtech Science KimWipes	Kimberly-Clark
NanoDropTM 2000c	Thermo Scientific
Terasaki Plates	Greiner Bio-One
TGX-Mini Protean Gradient SDS-PAGE System	Bio-Rad Laboratories
Millipore Milli-Q Water Purification System	Merck Millipore
Rigaku XtaLAB Synergy Flow XRD	Rigaku
Superdex^{TM}200 Increase Column	Cytiva

Appendix C
Protein Ladder

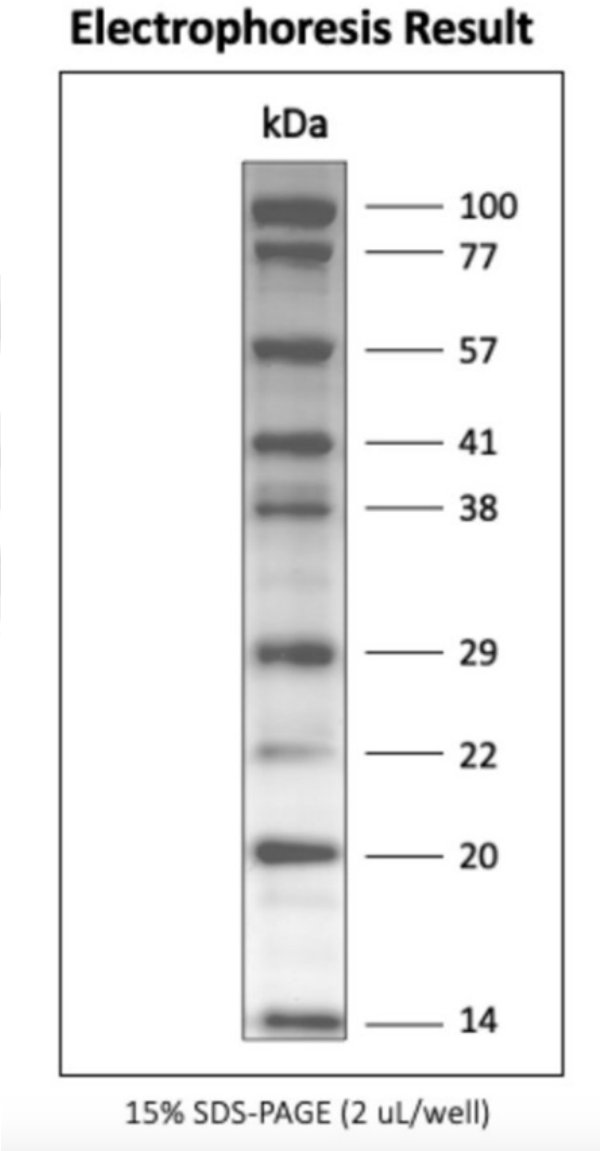

Figure C.1: KUYBIIG-M Protein ladder/

Appendix D
Crystallization Screening Solutions

3D Structure Screen	Molecular Dimensions
Additive Screen	Hampton Research
Clear Strategy Screen	Molecular Dimensions
CryoPro	Hampton Research
Crystal Screen	Hampton Research
Crystal Screen Cryo	Hampton Research
Detergent Screen	Hampton Research
Grid Screen Ammonium Sulfate	Hampton Research
Grid Screen MPD	Hampton Research
Grid Screen PEG/LiCl	Hampton Research
Grid Screen PEG6000	Hampton Research
Grid Screen Sodium Chloride	Hampton Research
Helix	Molecular Dimensions
Index	Hampton Research
Ionic Liquid Screen	Hampton Research
JBScreen Nuc-Pro	Jena Bioscience
JCSG	Molecular Dimensions
MacroSol	Molecular Dimensions
MembFac	Hampton Research
MIDAS	Molecular Dimensions
Morpheus	Molecular Dimensions
MultiXtal	Molecular Dimensions
Natrix	Hampton Research
NeXtal Protein Complex Suite	NeXtal Biotechnologies
NR-LBD	Molecular Dimensions

PACT Premier	Molecular Dimensions
PEG/Ion	Hampton Research
PEGRx	Hampton Research
PGA Screen	Molecular Dimensions
ProPlex Screen	Molecular Dimensions
Quick Screen	Hampton Research
SaltRx	Hampton Research
Structure Screen	Molecular Dimensions
Stura FootPrint Screen	Molecular Dimensions
Wizard	Rigaku
Wizard Cryo	Rigaku
Wizard Precipitant Synergy	Rigaku